ALMA MATER STUDIORUM
UNIVERSITÀ DI BOLOGNA

DIPARTIMENTO DI INGEGNERIA INDUSTRIALE

CORSO DI LAUREA IN
INGEGNERIA AEROSPAZIALE

DEVELOPMENT AND PERFORMANCE EVALUATION OF A HIGH-EFFICIENCY CANARD UAV

Tesi di laurea in Costruzioni Aerospaziali

Relatore

Prof. Enrico Troiani

Presentata da

Mattia Di Tota

Sessione Marzo 2026

Anno Accademico 2025/2026

ALMA MATER STUDIORUM
UNIVERSITÀ DI BOLOGNA

Abstract

This thesis presents the conceptual design, development, and performance evaluation of a subscale Unmanned Aerial Vehicle (UAV) optimized for high-efficiency, low-Reynolds-number flight. Designed primarily to enhance range and endurance, the vehicle adopts an unconventional canard configuration coupled with an electric pusher propulsion system.

The design methodology followed an iterative process, utilizing the Flow5 computational fluid dynamics solver, which adopts a 3D Panel Methods to also capture the interference phenomena characteristic of canard aircraft. A critical phase of the aerodynamic development involved mitigating the destructive downwash wake generated by the canard. This was achieved by introducing a vertical structural offset and adopting the cambered SD7037 airfoil for both lifting surfaces, reducing trim drag and preventing premature flow separation at low speeds.

To guarantee passive flight stability without the need for active control systems, the mass distribution was managed to secure a positive static margin of 13.86%. Lateral-directional stability was achieved through the integration of a 4° wing dihedral and a centrally mounted vertical stabilizer, successfully suppressing spiral divergence and lightly damping Dutch roll oscillations. The structural integrity of the airframe was validated through a CAD volumetric analysis, verifying that a lightweight semi-monocoque architecture utilizing balsa, plywood, and carbon fiber could easily withstand peak bending moments while adhering to the 1.280 kg Maximum Take-Off Weight constraint.

Numerical validation of the fully integrated vehicle, including fuselage interference and skin friction penalties, confirms that the UAV achieves an aerodynamic efficiency of 14.23 and a minimum sink rate of 1.12 m/s. Powered by a 100 W peak electrical system, the platform demonstrates a mission endurance, capable of either 37 minutes of continuous powered cruise or executing over 12 full climb-and-glide cycles.

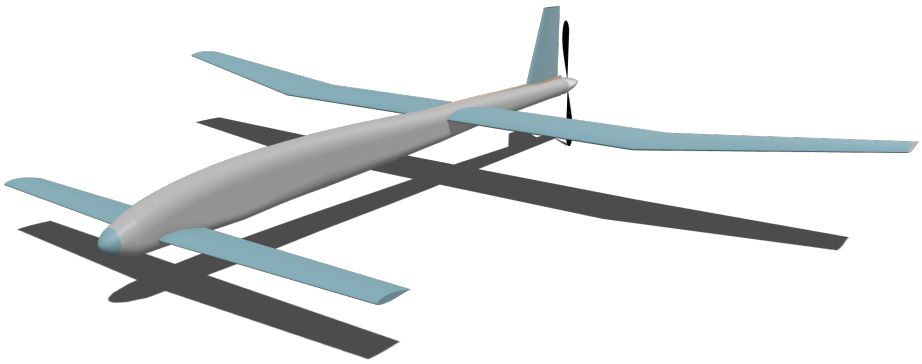

Figure 1: Final UAV design

Contents

1 Introduction **6**

1.1 Background and Motivation 6
1.2 Inspiration from Glider Configurations 6
1.3 Canard Configurations: Advantages and Challenges 6
1.4 Scope and Objectives of the Thesis 7
1.5 Methodology Overview 7

2 Mission Definition and Design Requirements **8**

2.1 Mission Profile and Operational Envelope 8
2.2 Performance Requirements 8
2.3 Stability and Controllability Requirements 9
2.4 Geometric, Mass, and Manufacturing Constraints 9

3 Conceptual Configuration Development **10**

3.1 Reference Aircraft and Preliminary Benchmarks 10
3.2 Initial Sizing Considerations 10
3.3 Trade-Off Analysis on Lifting Surface Layouts 10
3.4 Selection of the Final Global Configuration 11

4 Aerodynamic Design and Stability Analysis **12**

4.1 Main Wing Aerodynamic Design 12
4.1.1 Airfoil Selection 12
4.1.2 Planform Trade-off Analysis 14
4.1.3 Lateral Stability and Dihedral Integration 15
4.1.4 Wing Sizing Methodology 17
4.2 Canard Aerodynamic Design 18
4.2.1 Planform and Geometric Integration 18
4.2.2 Airfoil Selection and Trim Analysis 19
4.2.3 Performance Impact 20
4.3 Vertical Stabilizer and Lateral-Directional Stability 21
4.3.1 Aerodynamic Role and Dutch Roll Suppression 21
4.3.2 Geometry and Airfoil Selection 21
4.3.3 Longitudinal Placement 22
4.4 Mass Distribution, Neutral Point, and Static Margin 22
4.4.1 Mass Distribution and Center of Gravity 22
4.4.2 Neutral Point Determination 22
4.4.3 Static Margin Evaluation 23

4.5 Trim Condition and Sink Rate Estimation 23
4.5.1 Longitudinal Trim Selection 23
4.5.2 The Trim Angle Trade-off and Wake Impingement 23
4.5.3 Performance Estimation: Efficiency and Sink Rate 25

5 Numerical Aerodynamic Methods 29
5.1 Flow5 and VLM Methodology 29
5.1.1 Theoretical Framework: 3D Panel Method 29
5.1.2 Numerical Discretization: The Linear Galerkin Formulation 29
5.1.3 Viscous-Inviscid Interaction 30
5.2 Modeling Assumptions and Limitations 30
5.2.1 Assumptions 30
5.2.2 Limitations 31
5.3 Aerodynamic Coefficients Extraction 31
5.3.1 Force and Moment Normalization 31
5.3.2 Lift and Moment Calculation 32
5.3.3 Induced Drag Calculation 32
5.3.4 Viscous Drag Formulation 33
5.4 Neutral Point Determination 33
5.4.1 Derivative Calculation 33
5.4.2 Mathematical Extraction 33

6 Fuselage and Structural Integration 34
6.1 Aerodynamic Role of the Fuselage 34
6.1.1 Slenderness and Drag Minimization 34
6.1.2 The Destabilizing Pitching Moment 35
6.1.3 Multi-Surface Integration and Interference 35
6.1.4 Quantified Aerodynamic Impact of Fuselage Integration 35
6.2 Structural Layout and Load Paths 38
6.2.1 Spanwise Lift Distribution and Stall Safety 38
6.2.2 Bending Moment and Primary Spar Sizing 39
6.2.3 Torsional Loads and Rib Architecture 40
6.3 Fuselage Structural Layout and Component Integration 42
6.3.1 Semi-Monocoque Framework 42
6.3.2 Subsystem Packaging and CG Management 42
6.3.3 Lifting Surface Integration 43
6.4 Materials Selection and Manufacturing Considerations 45
6.4.1 Primary Load-Bearing Elements 45

6.4.2 Internal Skeleton . . . 45
6.4.3 Aerodynamic Skin . . . 45
6.4.4 Volumetric Analysis and Mass Budgeting . . . 46

7 Propulsion System Design 46
7.1 Electric Propulsion for Small UAVs . . . 46
7.2 Pusher Propeller Configuration Rationale . . . 47
7.3 Thrust and Power Requirements . . . 48
7.3.1 Fuselage Skin Friction Estimation . . . 48
7.3.2 Cruise Requirements . . . 48
7.3.3 Rate of Climb Requirements . . . 49
7.3.4 Electrical Power Sizing and Efficiency . . . 50
7.4 Motor and Propeller Matching . . . 51
7.4.1 Propeller Selection and Pitch Speed . . . 51
7.4.2 Brushless Motor Sizing (K_v Rating) . . . 51
7.5 Battery Sizing and Flight Endurance . . . 52
7.5.1 Total Energy Capacity . . . 52
7.5.2 Continuous Powered Cruise Endurance . . . 52
7.5.3 Climb and Glide Mission Profile . . . 53

8 Conclusions and System-Level Synthesis 53
8.1 Architecture Trade-Offs and Synthesis . . . 53
8.2 Summary of Achievements . . . 55
8.3 Limitations of the Current Study . . . 61
8.4 Future Work . . . 62

List of Figures

1 Final UAV Design . . . 1
2 Airfoils Polars . . . 13
3 Sink Rate and Efficiency Comparison between Planforms . . . 15
4 Root Locus Analysis . . . 16
5 Trim Condition Streamlines . . . 19
6 Sink Rate and Efficiency Comparison between Canard Airfoils . . . 20
7 Cm v Alpha . . . 24
8 Streamlines at a 4° Angle of Attack . . . 25
9 Final Configuration Polars . . . 26
10 Final Configuration Sink Rate and Efficiency at Trim . . . 27

11 Diagonal View of the Final Configuration 27
12 Upper View of the Final Configuration 28
13 Front View of the Final Configuration 28
14 Wing Panels 30
15 Fuselage 34
16 Fuselage Mesh 36
17 Final Configuration with Fuselage Polars 37
18 Local Lift Distribution 38
19 Bending Moment 39
20 Pitching Moment 40
21 Wing Internal Structure 41
22 Components Layout 43
23 Complete Internal Structure 44
24 D v Alpha in Cruise 49
25 Trimmed Climb Polars 50
26 Complete UAV Diagonal View 56
27 Complete UAV Upper View 57
28 Complete UAV Front View 57
29 Complete UAV Lateral View 58
30 Rendering 58

1 Introduction

1.1 Background and Motivation

The proliferation of Unmanned Aerial Vehicles (UAVs) has driven the need for platforms capable of extended flight endurance and maximized aerodynamic efficiency. However, developing efficient small scale UAVs introduces complex fluid dynamic challenges that preclude simply scaling down conventional, high-speed aircraft designs. The motivation of this thesis is to leverage these strategic aerodynamic advantages by developing, optimizing, and numerically validating an unconventional configuration for an UAV, achieving a delicate balance between aerodynamic efficiency and passive stability.

1.2 Inspiration from Glider Configurations

By mimicking the streamlined profiles of traditional sailplanes, UAVs can maximize their lift-to-drag (L/D) ratio, thereby reducing power consumption during cruise and extending their overall operational range. The defining aerodynamic feature of such a configuration is the use of a high aspect ratio wing. Increasing the aspect ratio minimizes the strength of wingtip vortices, which directly reduces lift induced drag. While full scale sailplanes can achieve glide ratios exceeding 50:1, small-scale UAVs must balance these aerodynamic ideals with structural realities and fluid dynamic constraints.[15]

1.3 Canard Configurations: Advantages and Challenges

The canard configuration represents a distinct departure from the conventional aft-tail layout, fundamentally altering the distribution of aerodynamic forces and stability mechanisms. A primary aerodynamic advantage of the canard is its active contribution to the total lift of the aircraft. In a traditional configuration, the horizontal stabilizer must often produce a downward force to balance the pitching-down moment of the cambered main wing, increasing the total load the main wing must support. Conversely, a lifting canard generates an upward force, sharing the weight of the vehicle with the main wing.[5] Another significant aerodynamic benefit is inherent passive stall safety. For longitudinal stability to be maintained, a canard must be sized and loaded to reach its critical angle of attack and stall before the main wing. When the foreplane stalls, it loses lift and naturally drops the aircraft's nose, thereby reducing the main wing's angle of attack and preventing it from entering a fully stalled state.

Despite these benefits, the canard configuration introduces complex aerodynamic challenges, related to multi surface interference. The forward lifting surface generates a trailing vortex system and a strong downwash field that directly impinges upon the main wing. This downwash reduces the effective angle of attack of the inboard sections of the main wing, distorting its spanwise lift distribution away from the optimal elliptical shape. Consequently, the aerodynamic

efficiency of the main wing is compromised, and the induced drag of the overall system increases. Furthermore, the requirement for the canard to stall first imposes a severe performance limitation on the vehicle's gliding capabilities. Because the foreplane must always operate at a higher lift coefficient than the main wing to ensure stability, the main wing can never be used at its absolute maximum lift coefficient ($C_{L_{max}}$). The canard itself also incurs an induced drag penalty due to its typically shorter span.

Finally, in the context of small scale aircraft, the canard surface operates at low Reynolds numbers. In this highly viscous regime, the boundary layer is particularly susceptible to laminar separation and the formation of laminar separation bubbles. These phenomena can lead to non-linear lift behavior, stall characteristics, and increases in profile drag on the foreplane.[10, 3]

1.4 Scope and Objectives of the Thesis

This thesis details the conceptual and preliminary aerodynamic design, stability assessment, and numerical evaluation of a small scale UAV. The core focus of the study is the implementation and optimization of a glider inspired canard architecture, prioritizing aerodynamic efficiency and passive stability.

Within this defined scope, the primary objectives of the thesis are as follows:

- **Mission Definition:** To define a coherent mission profile and corresponding aerodynamic requirements.
- **Aerodynamic Configuration and Sizing:** To design and optimize the geometry of the lifting surfaces, in order to maximize the vehicle's glide ratio and minimize the sink rate.
- **Interference Modeling:** To accurately capture and evaluate the aerodynamic interaction between the foreplane and the main wing, quantifying the effects of the canard downwash
- **Stability and Trim Verification:** To resolve the longitudinal instability risks of the canard layout, along with the lateral-directional one.

While propulsion and structural layout aspects are considered to ensure system coherence, they are treated as supporting elements rather than primary research topics.

1.5 Methodology Overview

The development of the UAV follows a structured and iterative design methodology consistent with classical aircraft design practices. The conceptual phase begins with the definition of mission requirements, which guides the selection of the overall configuration and targeted trade-off studies of airfoils and wing planforms. Subsequently, aerodynamic design and stability analyses are conducted through the Flow5 software. These tools are employed to evaluate lift, drag, pitching

moment behavior, trim conditions, and stability margins. By adjusting the aircraft parameters, the vehicle's geometry is continuously refined. Once a satisfactory aerodynamic baseline is achieved, additional analyses are performed to account for fuselage effects and propulsion integration.

2 Mission Definition and Design Requirements

2.1 Mission Profile and Operational Envelope

The UAV considered in this work is intended to operate as a small platform optimized for efficient, steady flight rather than high-speed or highly dynamic maneuvers. The reference mission profiles are characterized by an initial take-off phase, after which the vehicle can execute two distinct operational patterns depending on the mission requirements.

- **Range Oriented Mission:** It consists in a continuous climb to a target altitude followed by a sustained, powered steady-state cruise. The mission end with a glide phase to the ground.
- **Endurance Oriented Mission:** In this case, the UAV perform intermittent powered climbs alternated by unpowered glides. The mission ultimately concludes with a controlled descent and recovery.

The operational envelope is defined primarily by low Reynolds numbers, moderate angles of attack, and quasi-steady flight conditions.

2.2 Performance Requirements

The performance requirements are derived directly from the mission profile and are expressed in terms of measurable aerodynamic and flight mechanics quantities.

Endurance

Endurance is a primary performance driver for the UAV. While absolute endurance depends on battery capacity and propulsion efficiency, the aerodynamic design must minimize the power required to sustain flight. This translates into the requirement for low drag at cruise conditions and efficient lift generation at relatively low airspeeds.

Sink Rate

The sink rate represents a key indicator of aerodynamic efficiency, particularly for glider inspired configurations. A low sink rate implies reduced power demand in powered flight and improved

glide performance in unpowered conditions. The sink rate is evaluated at trimmed flight conditions and is used as a benchmark for comparing alternative aerodynamic configurations during the design process.

Cruise Efficiency

Cruise efficiency is defined in terms of the lift-to-drag ratio achieved at the nominal cruise condition. The UAV is required to operate at a stable trim point where the lift-to-drag ratio is sufficiently high to ensure efficient energy usage and minimal control effort.

2.3 Stability and Controllability Requirements

To guarantee safe and predictable flight without relying on active flight control systems, the UAV must satisfy strict passive aerodynamic stability criteria. These requirements govern the geometric sizing, lifting surface placement, and the permissible center of gravity envelope.

In the longitudinal plane, the primary requirement is inherent static stability, which is mathematically defined by a negative pitching moment derivative with respect to the angle of attack ($C_{m\alpha} < 0$). Because a canard acts as a destabilizing element since its aerodynamic center sits ahead of the CG, the overall aircraft CG must be positioned sufficiently forward of the vehicle's neutral point. An UAV requires a more robust positive static margin than a typical manned aircraft, typically targeting between 10% and 15% of the Mean Aerodynamic Chord.

From a controllability perspective, the aircraft must achieve longitudinal equilibrium ($C_m = 0$) an angle of attack that yields the optimal cruise lift-to-drag ratio.

Finally, the vehicle must fulfill lateral-directional stability criteria
($C_{l\beta} < 0$, $C_{n\beta} > 0$) to ensures a coordinated flight path without the need for active controls. [5]

2.4 Geometric, Mass, and Manufacturing Constraints

The design is subject to several geometric and mass constraints typical of small platforms. The overall size of the vehicle is limited to ensure ease of transportation, handling, and manufacturing. Wing span, fuselage length, and control surface dimensions must remain compatible with small scale construction techniques and available materials.

The total mass of the UAV is constrained by propulsion capability and structural considerations. A lightweight configuration is required to maintain low wing loading, which directly benefits aerodynamic efficiency and sink rate. At the same time, sufficient structural strength must be ensured to withstand aerodynamic loads and handling stresses.

Finally, the mass distribution must allow for a feasible center of gravity location compatible with longitudinal stability requirements, while accommodating propulsion, energy storage, avionics, and payload within the fuselage.

3 Conceptual Configuration Development

3.1 Reference Aircraft and Preliminary Benchmarks

The conceptual development of the Unmanned Aerial Vehicle is rooted in the aerodynamic evaluation of existing glider architectures and canard platforms.

Historically, the application of the canard configuration to soaring aircraft is best exemplified by the Rutan Solitaire, a self launching sailplane. The Solitaire demonstrated that a canard layout could achieve high aerodynamic efficiency, recording a lift-to-drag ratio (L/D) of approximately 32:1.

Furthermore, it successfully validated the passive safety benefits of the architecture; by designing the foreplane to reach its critical angle of attack and stall prior to the main wing, the aircraft exhibited strong resistance to departure and deep stall conditions. [14]

However, transitioning from full-scale sailplanes to the small UAVs domain introduces severe scale effects. For this reason, rather than replicating a specific existing design, the reference analysis is used to establish realistic performance targets and identify configuration trends compatible with small UAVs.

3.2 Initial Sizing Considerations

At this stage, sizing is performed only at a conceptual level, aiming to define reasonable proportions rather than final dimensions.

The preliminary sizing of the UAV was driven by a combination of operational handling constraints and the aerodynamic necessity to minimize induced drag during the unpowered glide phase. To ensure that the aircraft remained easily transportable and practical for small-scale manufacturing, the maximum wingspan (b) was strictly constrained to 1.20 m.

To achieve the high aerodynamic efficiency characteristic of sailplanes, an initial target Aspect Ratio (AR) of 12 was selected. Utilizing the fundamental geometric relationship for wing sizing ($S = b^2/AR$), the preliminary reference area (S) for the main wing was estimated. Substituting the defined span and target aspect ratio into this equation yielded a baseline wing area of 0.12 m^2, which function as the starting geometric boundary for the computational optimization phase.

Concurrently, an initial mass budget was established to determine the required lift capabilities. The Maximum Take-Off Weight (MTOW) of the vehicle was constrained to 1.28 kg, which accounts for the internal payload, avionics, and the structural mass of the airframe.

3.3 Trade-Off Analysis on Lifting Surface Layouts

Following the selection of the canard architecture, a trade-off analysis was required to define the specific geometric layout of the lifting surfaces. In a canard configuration, the design parameters of the foreplane and main wing cannot be optimized in isolation; their aerodynamic coupling

necessitates compromises between induced drag minimization, structural mass, and longitudinal stability.

The primary trade-off in canard sizing involves the span and area ratios between the two surfaces. As stated in chapter 1.3, the canard must operate at a higher lift coefficient than the main wing. Because induced drag is proportional to the square of the lift coefficient, a heavily loaded, short-span canard generates a disproportionately level of induced drag. While increasing the canard's span improves its aerodynamic efficiency and reduces the intensity of its trailing tip vortices, it simultaneously shifts the aircraft's global aerodynamic center forward, which reduces the static margin and requires additional nose ballast to correct. Consequently, a moderate area ratio was selected, utilizing a 0.60 m span to provide sufficient pitch trim authority without incurring an excessive structural weight penalty.[10]

For the main wing planform, four geometric alternatives were evaluated: fully rectangular, fully tapered, partially tapered, and winglet-equipped designs. A fully rectangular wing offered maximum build simplicity but suffered from poor aerodynamic efficiency due to massive tip vortices. A fully tapered wing offered the best approximation of an elliptical lift distribution and the lowest induced drag, but presented manufacturing complexities at a small scale. The optimal compromise was determined to be a partially tapered planform. By keeping the inboard section rectangular and tapering only the outer panels, the design achieves a near-elliptical spanwise loading while providing sufficient root chord thickness for structural spar integration. [13, 2]

Finally, a trade-off was conducted regarding lateral-directional stability devices. While winglets were considered to simultaneously reduce induced drag and provide directional stability, they inherently add structural mass at the extremities of the wingspan, increasing the roll moment of inertia. Furthermore, at low Reynolds numbers, the sharp junctions of winglets can trigger localized flow separation. Therefore, the design discarded winglets in favor of a single, centrally mounted vertical stabilizer. Paired with the 4° dihedral of the main wing, this conventional fin provides the necessary aerodynamic yaw damping to suppress Dutch roll oscillations with minimal structural complexity. [5, 12]

3.4 Selection of the Final Global Configuration

The culmination of the conceptual design phase results in the definition of the final global architecture of the UAV. This baseline configuration serves as the geometric foundation that will undergo detailed numerical optimization and stability analysis in the subsequent design phases.

At this stage, the vehicle is defined as a canard monoplane with a pusher propulsion system. The pusher configuration is selected because it ensures that the main wing operates entirely in clean, undisturbed freestream air, which is critical for minimizing profile drag.

A single, centrally mounted vertical stabilizer is located at the aft of the fuselage to provide directional stability and suppress lateral-directional oscillations.

Regarding the lifting surfaces, while a partially tapered main wing planform has been preliminarily selected to balance aerodynamic efficiency with manufacturing simplicity, this decision serves as a conceptual baseline. The final geometric definition of the wing planform will be established only after quantitative aerodynamic validation.

The macroscopic parameters frozen at the end of this conceptual phase include a maximum wingspan of 1.20 m, an initial aspect ratio target of 12, and a Maximum Take-Off Weight (MTOW) of 1.280 kg. This global configuration provides a passively stable platform that is now prepared for detailed lifting surface design and numerical validation.

4 Aerodynamic Design and Stability Analysis

4.1 Main Wing Aerodynamic Design

The wing represents the primary lifting surface and was therefore sized and optimized to maximize aerodynamic efficiency while ensuring compatibility with the canard configuration and the global stability requirements.

The main design targets for the wing are:

- High aerodynamic efficiency
- Low sink speed
- Predictable stall behavior
- Compatibility with a canard
- Structural simplicity and manufacturability

4.1.1 Airfoil Selection

The selection of the airfoil was conducted through a comparative analysis between low-Reynolds profiles suitable for glider applications.

In particular, the SD7037 and E393 airfoils were evaluated.

The comparison focused on:

- Lift coefficient at low angles of attack
- C_L/C_D ratio at the expected trim condition
- Stall characteristics
- Sensitivity to surface imperfections

Comparing the polars of these profiles (Figure 2) on Airfoils tools before running any simulation, shows that, at the speed of reference and low angle of attack, the SD7037 airfoil had better and more stable behaviors than the E393. [1]

As a matter of fact, Flow5 simulations showed that, although both airfoils exhibited acceptable performance, the SD7037 provided a more favorable lift-to-drag ratio in the operational range of interest, together with smoother stall behavior. For these reasons, the SD7037 airfoil was selected for the main wing.

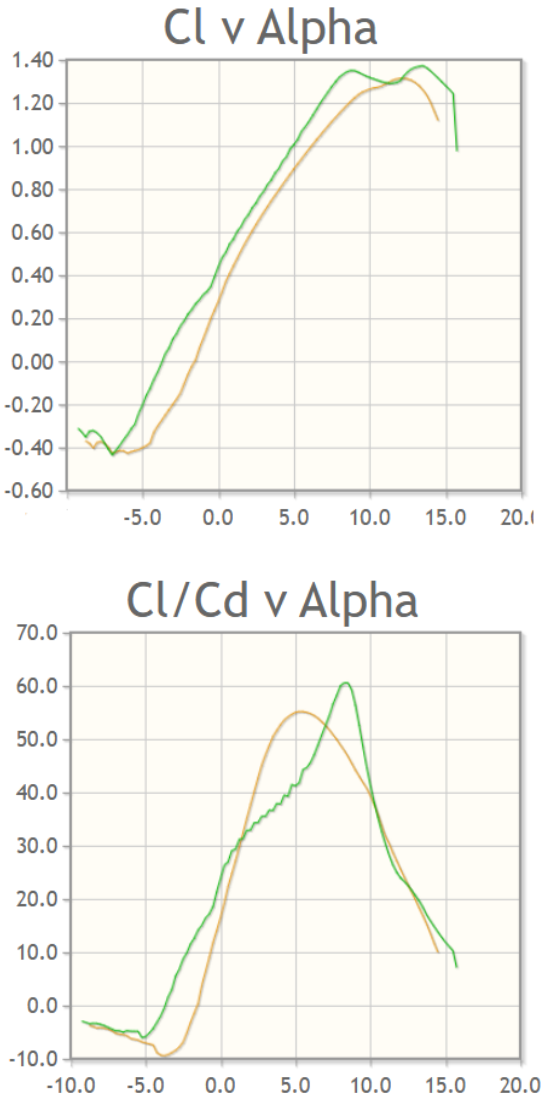

Figure 2: C_L v Alpha and C_L/C_D v alpha, in green E393 in yellow SD7037

4.1.2 Planform Trade-off Analysis

Following the airfoil selection, the wing planform was defined through a trade-off analysis. The goal was to balance aerodynamic efficiency, Span Efficiency Factor (e), manufacturability and stability integration.

Three primary configurations were evaluated:

1. **Rectangular Planform:** This configuration offered the highest manufacturing simplicity. However, it suffers from a lift distribution point of view, leading to stronger wingtip vortices and increased induced drag. Furthermore, integrating a dihedral angle into a constant chord structure presents structural joining challenges.

2. **Fully Tapered Planform:** While aerodynamically superior due to its approximation of an elliptical lift distribution, a fully tapered wing introduces significant manufacturing complexity and structural fragility at the narrow wingtips.

3. **Partially Tapered Planform:** This hybrid configuration features a constant chord root section and tapered outer panels. It was identified as the optimal compromise.

Quantitative Performance Snapshot: To validate the selection, a direct numerical comparison was conducted between the rectangular and partially tapered configurations at the design trim condition (Figure 3). The results are summarized below:

- **Rectangular Planform:**
  - Sink Rate ≈ 0.84 m/s
  - Efficiency $L/D \approx 17.68$
- **Partially Tapered Planform:**
  - Sink Rate ≈ 1.12 m/s
  - Efficiency $L/D \approx 17.52$

The simulation results indicated a negligible difference in pure aerodynamic performance.

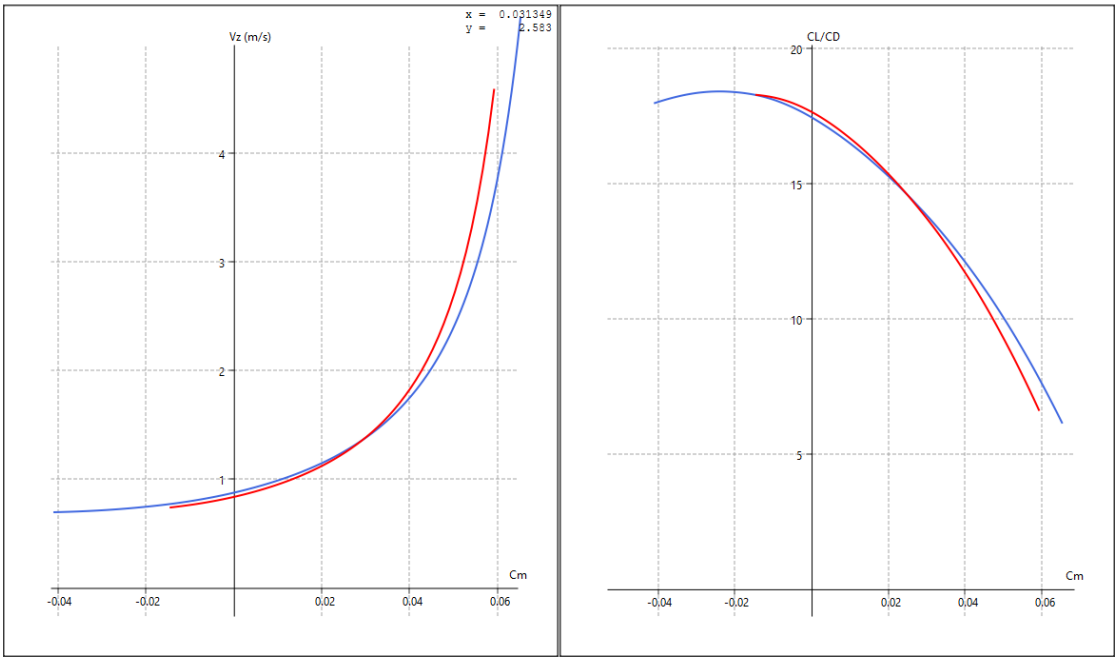

Figure 3: V_z v C_m and C_L/C_D v C_m, in blue the partially tapered configuration in red the rectangular configuration

4.1.3 Lateral Stability and Dihedral Integration

A critical requirement for the UAV is passive lateral stability. Without active aileron control for every minor disturbance, the vehicle must possess an inherent tendency to level its wings. To achieve this, a positive dihedral angle of 4° was integrated into the design. In a sideslip condition, this dihedral geometry generates a restoring rolling moment ($C_{l\beta} < 0$), allowing the aircraft to self-correct for roll disturbances. Numerical stability checks (Root Locus analysis) confirmed that this dihedral angle stabilizes the spiral mode without inducing excessive roll-yaw coupling (Dutch roll).[5]

Root Locus Analysis:

The selection of the dihedral angle was validated through a comparative Root Locus analysis (Figure 4) between the planar (no dihedral) and the final (4° dihedral) configurations. The analysis of the eigenvalues revealed the following behaviors:

- **Roll Mode (Subsidence):** In both configurations, the Roll Mode root was located on the negative real axis. With the introduction of the 4° dihedral, this root exhibited a minor but noticeable shift to the left compared to the baseline case. While the magnitude of this displacement was not large, it represents a definitive improvement in the time constant for roll subsidence, enhancing the aircraft's passive tendency to resist spiral divergence.

- **Dutch Roll Mode:** The Dutch Roll mode (complex conjugate pair) remained largely invariant. In the dihedral configuration, the roots moved slightly closer to the imaginary axis and marginally higher, indicating a slight increase in frequency. However, this variation was significantly smaller than the shift observed in the Roll Mode.

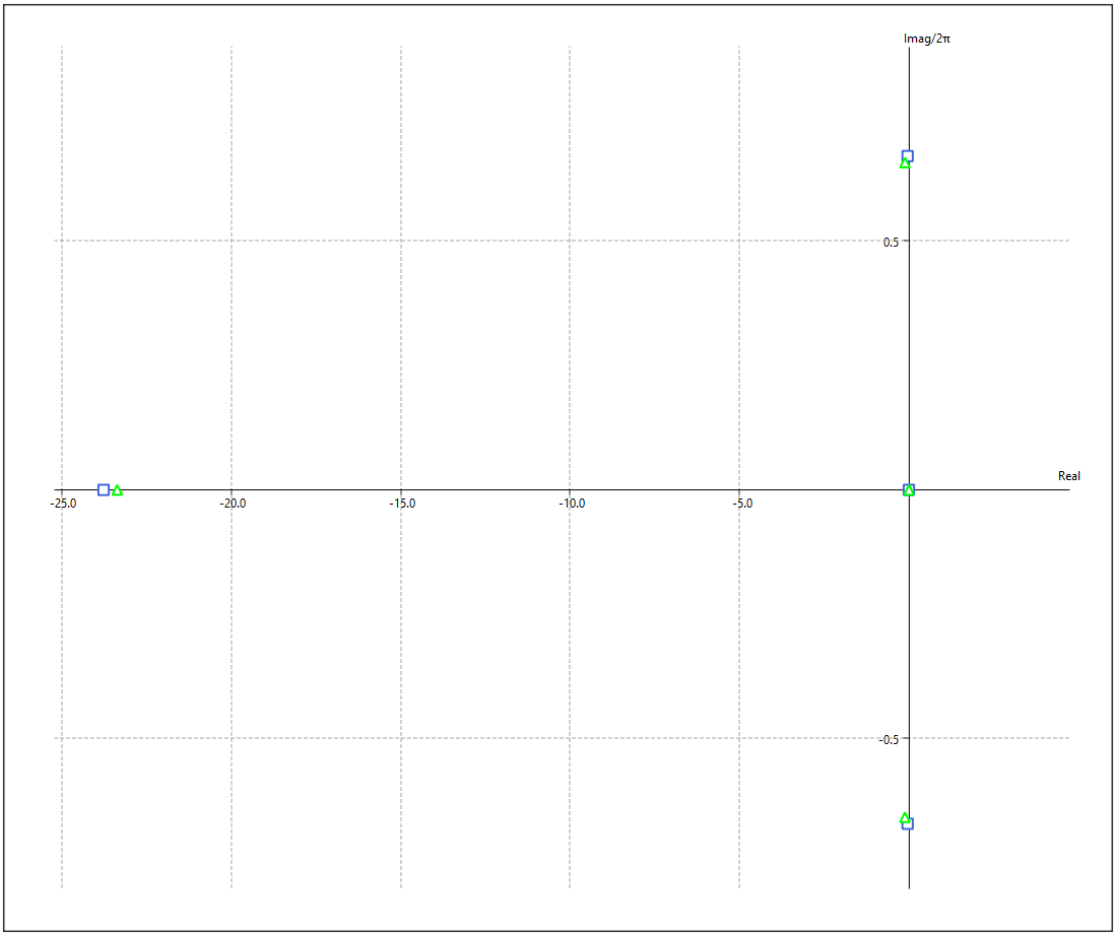

Figure 4: Root locus analysis, in blue the dihedral configuration in green the planar one

Time-Domain Validation of the Trade-off: To quantify this trade-off and validate the handling qualities, time-domain stability simulations were performed using Flow5. The modal response for the Roll Subsidence mode (Mode 1) confirmed a highly stable, non-oscillatory aerodynamic response. When subjected to an initial roll displacement, the aircraft exhibited a rapid exponential decay. The restoring moment of the 4° dihedral arrested the roll rate and returned the roll angle to equilibrium in less than 0.3 seconds, ensuring the UAV actively resists spiral divergence.

Conversely, the simulation of the Dutch Roll mode (Mode 3) highlighted the cost of this

dihedral. As anticipated, the response is characterized by a coupled yaw-roll oscillation. While the amplitudes of all state variables strictly converge toward zero over a 30-second period, proving the mode is dynamically stable, it is notably lightly damped. Comparative simulations of the planar baseline (0° dihedral) revealed a more damped Dutch roll behavior. The 4° dihedral inherently increased the rolling moment due to sideslip ($C_{l\beta}$), which aerodynamically opposes the directional stability ($C_{n\beta}$), thereby reducing the overall damping ratio.[5]

Design Conclusion: This lightly damped Dutch roll represents a conscious and necessary aerodynamic compromise for the main wing. For an unpowered autonomous glider, poor roll subsidence is highly dangerous and can lead to unrecoverable steep spirals. A lightly damped but stable Dutch roll is a benign characteristic that results in a temporary oscillation during gust recovery. Therefore, the 4° dihedral was retained: it sacrifices a fraction of Dutch roll damping to secure the aggressive, roll stability required for the mission profile.[15]

4.1.4 Wing Sizing Methodology

The sizing of the main wing was carried out following a performance-driven iterative approach. The preliminary sizing in chapter 3 provided an initial estimate of the wing surface, which was then refined through successive aerodynamic analyses.

The objective of this process was not solely to match the target aspect ratio, but to identify a configuration that simultaneously ensured:

- favorable lift-to-drag ratio,
- stable pitching behavior in combination with the canard,
- acceptable trim conditions,
- robustness with respect to mass distribution uncertainties.

The final chord dimensions, extracted from the Flow5 model, are:

- root chord $c_{\text{root}} = 0.11$ m,
- tip chord $c_{\text{tip}} = 0.06$ m.

Once a geometrical configuration satisfying the performance and stability criteria was identified, the resulting wing parameters were extracted. The final wing geometry is characterized by:

- a wingspan of approximately 1.2 m,
- a wing reference area $S = 0.117$ m^2,
- a mean aerodynamic chord $MAC = 0.100$ m,

- a wing incidence angle of $-0.4°$

The resulting aspect ratio, computed from the final geometry, is therefore:

$$AR = \frac{b^2}{S} \approx \frac{1.2^2}{0.117} \approx 12.3$$

which is in close agreement with the initial design target.

This sizing strategy ensured consistency between preliminary analytical expectations and numerical aerodynamic results. By relying on Flow5 simulations to refine the wing dimensions, the final geometry naturally embeds stability and performance consideration.

4.2 Canard Aerodynamic Design

Following the selection of the canard configuration, the aerodynamic design of the foreplane focused on minimizing the specific drag penalties inherent to this layout.

4.2.1 Planform and Geometric Integration

To mitigate the induced drag generated by the high spanwise loading of the foreplane, the design changed from a simple rectangular baseline to a slightly tapered planform. This geometry reduces the strength of the tip vortices, which is particularly important given the potential for wake ingestion by the main wing downstream.

Furthermore, The canard generates a trailing vortex sheet that induces a strong downwash field downstream. If the canard and the main wing are coplanar, this downwash impinges directly upon the inboard sections of the main wing, drastically reducing its effective angle of attack and consequently the efficiency.

To mitigate this interference, a vertical offset of 0.04 m was introduced, mounting the main wing in a high position relative to the canard's wake. Flow5 analysis (Figure 5) confirmed that this separation effectively protects the inboard wing sections from the majority of the foreplane's wake. [7]

The final geometric parameters for the canard are:

- Root/Mid Chord: 0.070 m
- Tip Chord: 0.055 m
- Span: 0.60 m
- Vertical Offset: 0.04 m (relative to the main wing root)

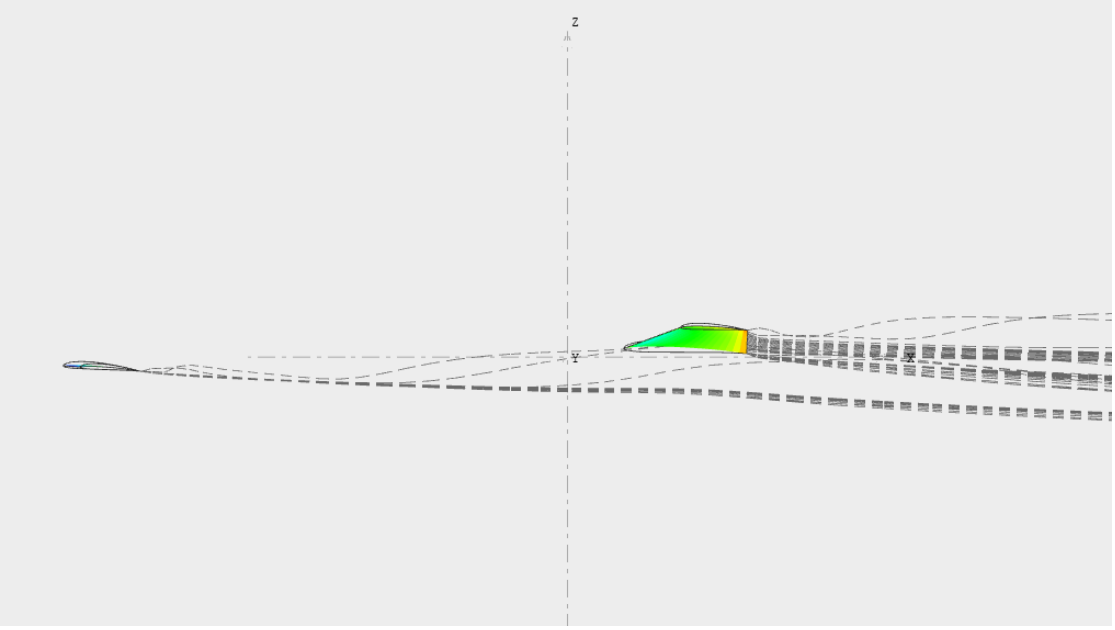

Figure 5: Streamlines obtained by a VLM analysis

4.2.2 Airfoil Selection and Trim Analysis

The selection of the canard airfoil was driven by a quantitative analysis of the trim requirements. The objective was to identify a profile capable of sustaining the required lift for longitudinal equilibrium without triggering premature flow separation.

Two distinct airfoil concepts were evaluated:

1. **Symmetric Baseline (NACA 0012-34):** A standard choice for all-moving control surfaces.
2. **High-Lift Cambered (SD7037):** The same cambered airfoil profile selected for the main wing.

Trim Setting Comparison: Simulations were conducted to determine the required canard geometric incidence setting to trim the complete aircraft. In both configurations, the global trim angle of attack of the aircraft (α_{trim}) was established at approximately 2.8°. However, achieving this equilibrium required different canard settings:

- **Symmetric NACA 0012:** Required a high geometric incidence of 4.7° relative to the fuselage.
- **Cambered SD Airfoil:** Required a geometric incidence of only 1.2°.

Aerodynamic Behavior: The analysis of the Flow5 polar graphs revealed that the symmetric NACA configuration exhibited unpredictable and non-linear aerodynamic behavior. This instability is directly attributable to the elevated 4.7° incidence angle required for trim. At the operational low-Reynolds numbers, forcing a symmetric profile to such high local angles of attack induces premature boundary layer separation. Conversely, the SD airfoil exploits its camber to generate the required lifting force at lower geometric incidence (1.2°), maintaining the flow attached and ensuring a robust stall margin.[2]

4.2.3 Performance Impact

The aerodynamic superiority of the cambered foreplane translated directly into measurable performance gains. A performance snapshot comparing the configurations (Figure 6), both utilizing the partially tapered main wing, at the $\alpha \approx 2.8°$ trim condition highlights this impact:

- **Aircraft with NACA Canard:**
  - Aerodynamic Efficiency (L/D): 16.031
  - Sink Rate (V_z): 0.97 m/s
- **Aircraft with SD Canard (Final Selection):**
  - Aerodynamic Efficiency (L/D): 17.460
  - Sink Rate (V_z): 0.88 m/s

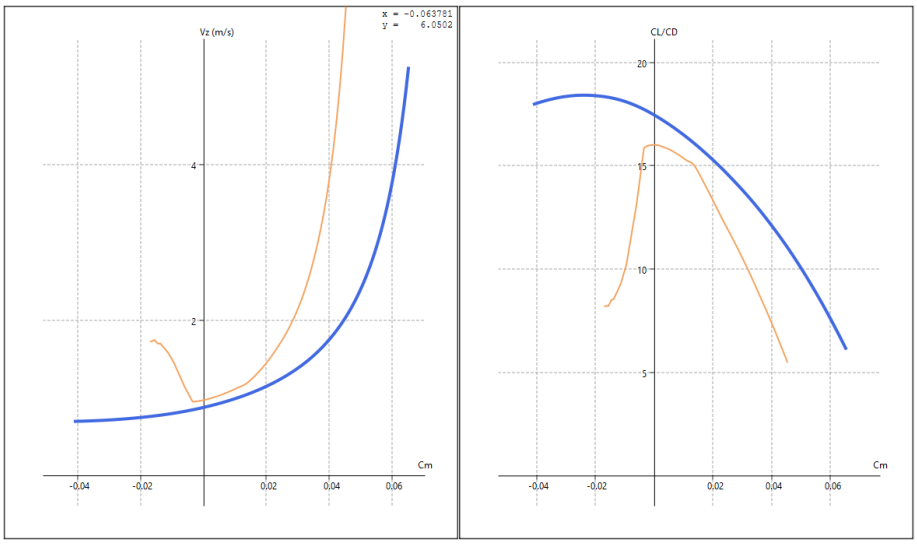

Figure 6: V_z v C_m and C_L/C_D v C_m, in blue the SD7037 configuration in YELLOW the NACA configuration

Conclusion: The integration of the SD airfoil on the canard improves the global efficiency and longitudinal balance of the UAV. By reducing the required trim incidence, it prevents flow separation on the foreplane, stabilizing the pitching moment behavior and improving the aircraft lift-to-drag ratio. Consequently, the SD airfoil was selected for the canard design.

4.3 Vertical Stabilizer and Lateral-Directional Stability

The vertical stabilizer plays a fundamental role in ensuring directional stability and providing adequate aerodynamic yaw damping. This is particularly critical in the present configuration due to the aerodynamic coupling introduced by the main wing's geometry.

4.3.1 Aerodynamic Role and Dutch Roll Suppression

The positive 4° dihedral angle adopted on the main wing is beneficial for static lateral stability, generating a strong restoring rolling moment ($C_{l\beta} < 0$) in response to sideslip. However, this dihedral introduces a strong coupling between the yaw and roll axes.

To counteract this instability, a single central vertical stabilizer was integrated into the aft section of the airframe, with the purpose of provide a restoring yawing moment proportional to the sideslip angle ($C_{n\beta} > 0$). As confirmed by the Root Locus analysis discussed in Section 4.1.3, the sizing and placement of the vertical stabilizer maintain the Dutch roll complex conjugate roots in the stable left-half plane, providing sufficient passive damping to suppress oscillatory tendencies.[5]

4.3.2 Geometry and Airfoil Selection

The geometric parameters of the vertical stabilizer were optimized through Flow5 simulations to evaluate steady flight and transient sideslip conditions. The goal was to guarantee stability without oversizing the component, which would increase skin friction drag and structural mass at the rear of the aircraft.

The finalized vertical stabilizer geometry is defined as follows:

- Airfoil: NACA 0012-34 (Symmetric)
- Span: 0.10 m
- Root Chord: 0.10 m
- Tip Chord: 0.06 m
- Vertical Offset: +0.04 m (relative to the main wing)

Airfoil and Planform Justification: A symmetric NACA 0012-34 airfoil was selected to ensure a linear aerodynamic response at small sideslip angles and to guarantee zero lateral

lift generation during coordinated, straight cruise. This tapering reduces the surface area and structural mass at the tip, lowering the moment of inertia around the roll axis.

4.3.3 Longitudinal Placement

The effectiveness of the vertical stabilizer depends on its moment arm relative to the vehicle's center of gravity. Positioned slightly aft of the main wing at the specific geometric coordinates $(x, y, z) = (0.30, 0, 0.05)$ m, the stabilizer's aerodynamic center leverages a sufficient moment arm with respect to the center of gravity ($x_{CG} = -0.051$ m), achieving the required directional control authority.

4.4 Mass Distribution, Neutral Point, and Static Margin

The longitudinal static stability and correct trim behavior of an aircraft are highly sensitive to the relative positioning of the Center of Gravity (CG) and the aerodynamic Neutral Point (NP).

4.4.1 Mass Distribution and Center of Gravity

The estimation of component masses was performed to allow an accurate placement of the center of gravity. Each component was modeled as a concentrated point mass located at its corresponding aerodynamic center or representative geometric position. This approach is appropriate for preliminary and conceptual design stages and allows direct integration with aerodynamic simulations.

The adopted mass distribution is summarized as follows:

- Main wing: 0.20 kg, located at $x = +0.099$ m; $z = 0.016$ m
- Canard: 0.10 kg, located at $x = -0.417$ m; $z = 0.029$ m
- Vertical stabilizer: 0.08 kg, located at $x = +0.355$ m; $z = 0.092$ m
- Structure and onboard systems: 0.90 kg, located at $x = -0.081$ m

The resulting total mass of the vehicle is 1.280 kg. From this distribution, the center of gravity was computed using Flow5, obtaining a CoG position of:

$$(x_{CG}, y_{CG}, z_{CG}) = (-0.051, 0, 0.006) \text{ m}$$

4.4.2 Neutral Point Determination

The neutral point (NP) of the complete configuration was determined numerically using Flow5, through the variation of the pitching moment coefficient with angle of attack, accounting for the combined aerodynamic contribution of the main wing, canard, and vertical stabilizer. The resulting neutral point location is:

$$x_{NP} = -0.04 \text{ m}$$

4.4.3 Static Margin Evaluation

The primary metric for quantifying longitudinal static stability is the Static Margin (SM), which expresses the normalized distance between the Neutral Point and the Center of Gravity. For the aircraft to exhibit passive longitudinal stability, the CG must be located forward of the NP, resulting in a positive static margin.

Using the Mean Aerodynamic Chord ($MAC = 0.100$ m) of the main wing as the reference length, the static margin is calculated as follows:

$$SM = \frac{x_{NP} - x_{CG}}{MAC}$$

Substituting the CG and NP positions obtained above, the static margin is:

$$SM = \frac{-0.04 - (-0.051)}{0.10} = 0.0991 \quad \Rightarrow \quad 9.91\%$$

Discussion

The resulting static margin confirms that the mass distribution and aerodynamic layout are well balanced. The center of gravity is positioned sufficiently ahead of the neutral point to guarantee stability, without being excessively forward, which would otherwise increase control effort and reduce aerodynamic efficiency. The resulting configuration therefore provides a robust basis for the analysis of trimmed flight conditions and sink rate estimation, which are addressed in the following section.

4.5 Trim Condition and Sink Rate Estimation

The ultimate objective of the aerodynamic and stability design phase is to establish a longitudinal equilibrium (trim) that maximizes cruise efficiency and endurance, while preserving sufficient control margins for maneuvering and turbulence recovery. This is evaluated through the pitching moment coefficient $C_m(\alpha)$, identifying the point where the net pitching moment acting on the aircraft is zero ($C_m = 0$).

4.5.1 Longitudinal Trim Selection

For the final configuration, the nominal cruise trim condition was established at a global angle of attack of $\alpha_{trim} = 2.85°$ (Figure 7), with a canard geometric incidence setting of 1.2° relative to the fuselage datum.

4.5.2 The Trim Angle Trade-off and Wake Impingement

Because the canard is an all-moving surface, it is theoretically possible to trim the aircraft at higher global angles of attack (e.g., $\alpha_{trim} \geq 4°$) by further increasing the canard's incidence. While mathematical models might suggest competitive Lift-to-Drag ratios at these higher angles, selecting such a condition as the nominal baseline introduces two critical aerodynamic liabilities:

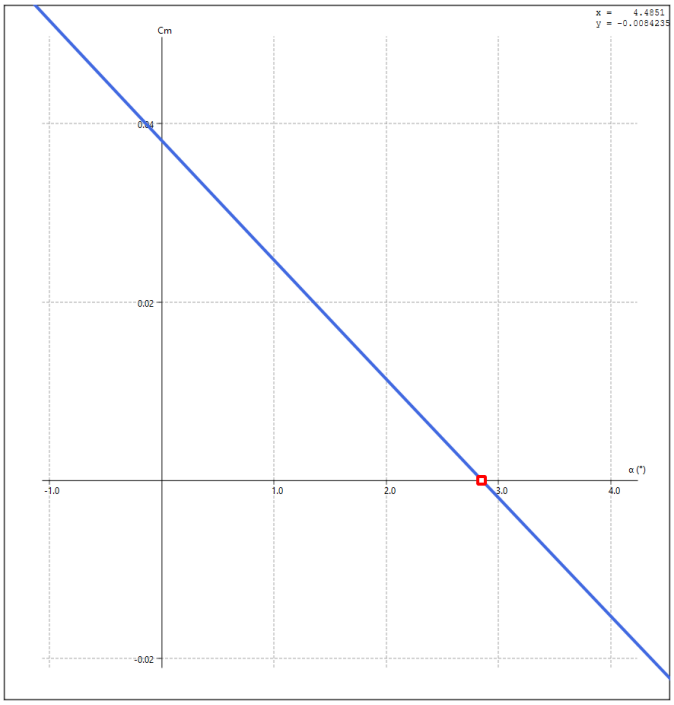

Figure 7: Cm v Alpha

1. **Reduction of Maneuver Margin:** In a canard architecture, passive safety mandates that the foreplane must stall before the main wing. If the aircraft is trimmed at a high baseline angle of attack (e.g., 4°), the canard is forced to operate close to its critical stall boundary simply to maintain level flight. If the flight controller were to command a pitch-up maneuver to initiate a climb, the required increase in incidence would leave virtually no stall margin, risking a sudden loss of lift on the foreplane. Trimming at 2.85° preserves a robust operational buffer.

2. **VLM Wake Interference:** Supplementary analyses conducted using the Vortex Lattice Method (VLM) revealed a highly sensitive interference phenomenon regarding the canard's downwash. At the chosen trim angle of 2.85°, the 0.04 m vertical offset separates the canard's wake from the main wing. However, the VLM flow field visualization (Figure 8) indicated that at higher angles of attack (such as 4°), the more loaded canard generates more tip vortices. This altered trajectory causes the turbulent wake to impinge directly onto the leading edge and upper surface of the main wing, disrupting the spanwise lift distribution. By limiting the nominal trim to $\alpha = 2.85°$, the design avoids this wake impingement regime, ensuring the main wing operates in clean, undisturbed airflow.

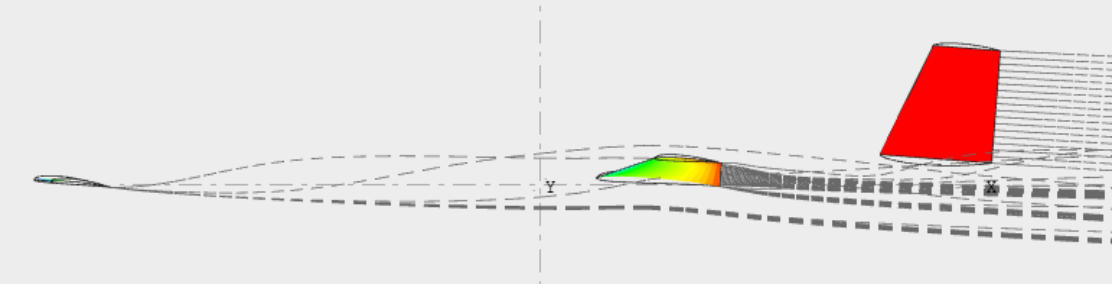

Figure 8: Streamlines at a 4° angle of attack

4.5.3 Performance Estimation: Efficiency and Sink Rate

Operating at the optimal 2.85° trim condition, the steady-state aerodynamic characteristics of the UAV were extracted from Flow5 (Figure 9). The specific coefficients at trim are:

- **Lift Coefficient** (C_L): 0.741
- **Drag Coefficient** (C_D): 0.042
- **Aerodynamic Efficiency** (L/D): 17.460

In unpowered flight, the sink speed is inversely proportional to the endurance parameter $\left(\frac{C_L^{3/2}}{C_D}\right)$ and is modeled by the relation.[5] For this final configuration, the aerodynamic endurance parameter and the sink rate evaluates to (Figure 10) :

- **Sink Rate** (V_z): 0.88 m/s
- **Endurance Parameter** $\left(\frac{C_L^{3/2}}{C_D}\right)$: 15.18

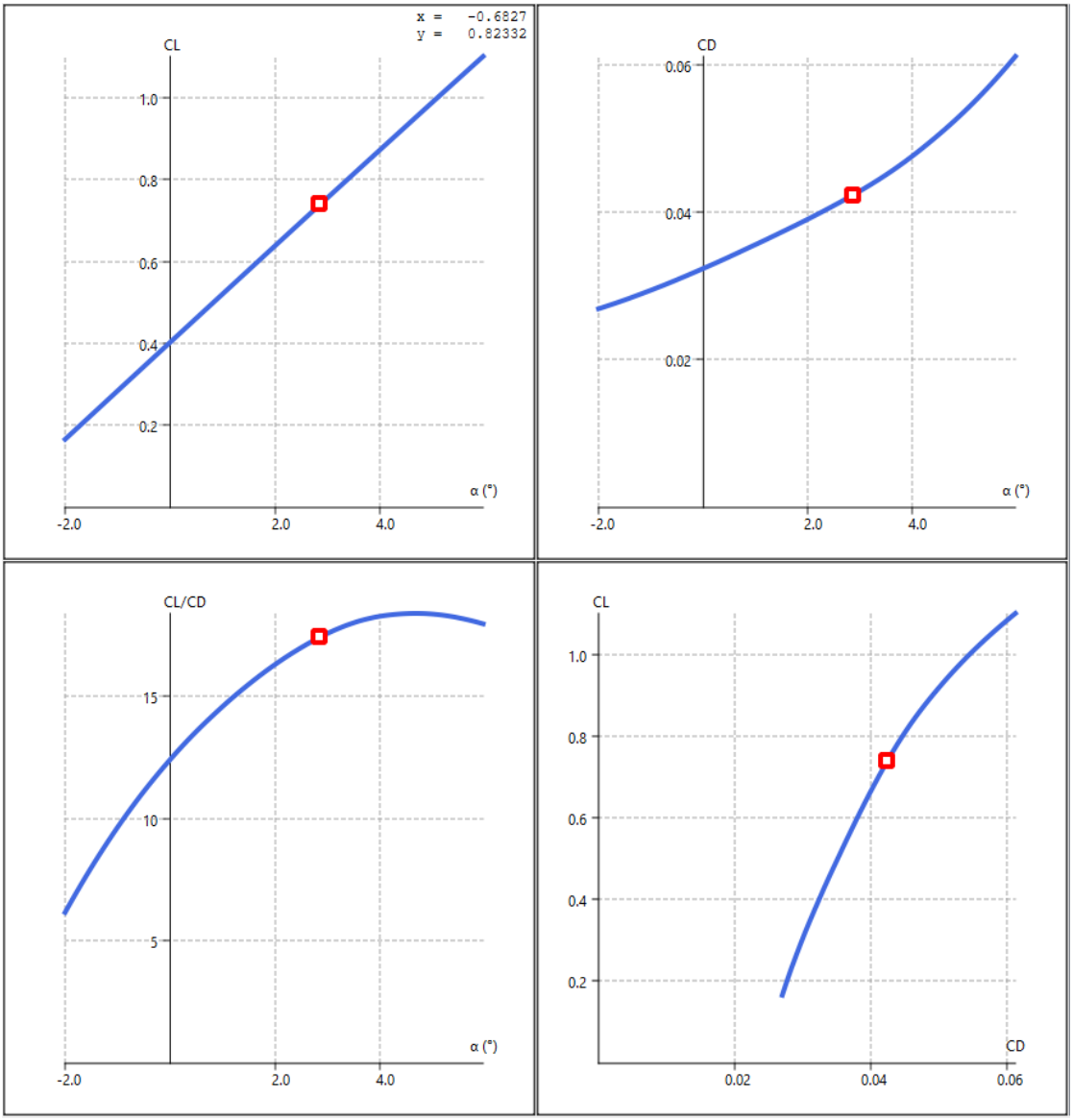

Figure 9: 1. C_L v Alpha 2. C_D v Alpha 3. C_L/C_D v Alpha 4. C_L v C_D

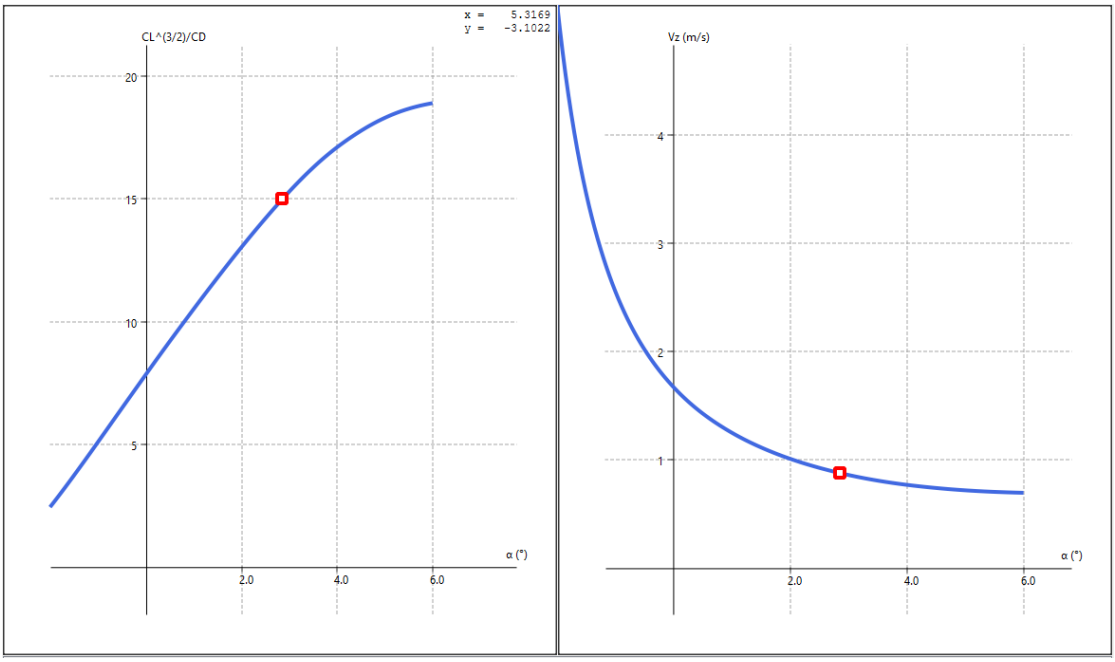

Figure 10: $\left(\frac{C_L^{3/2}}{C_D}\right)$ v Alpha and V_z v Alpha

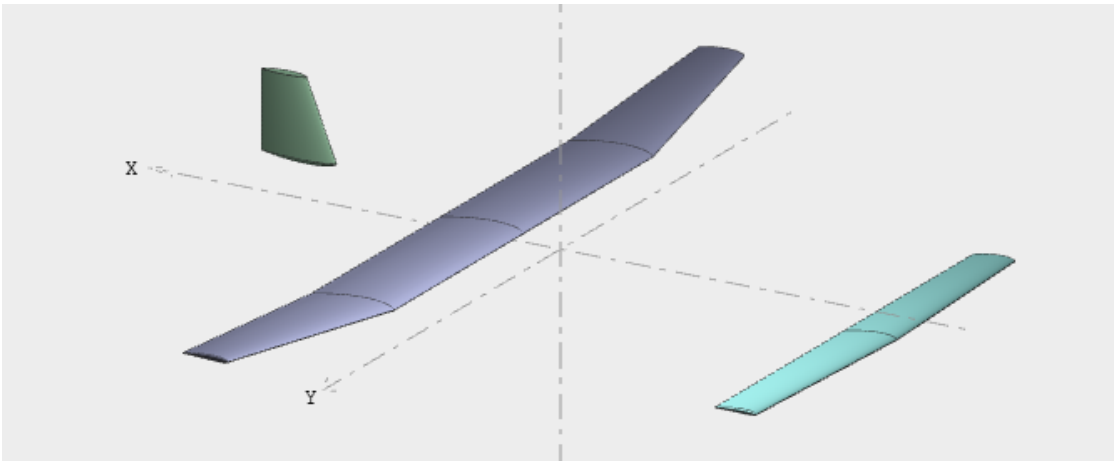

Figure 11: Diagonal view of the final configuration

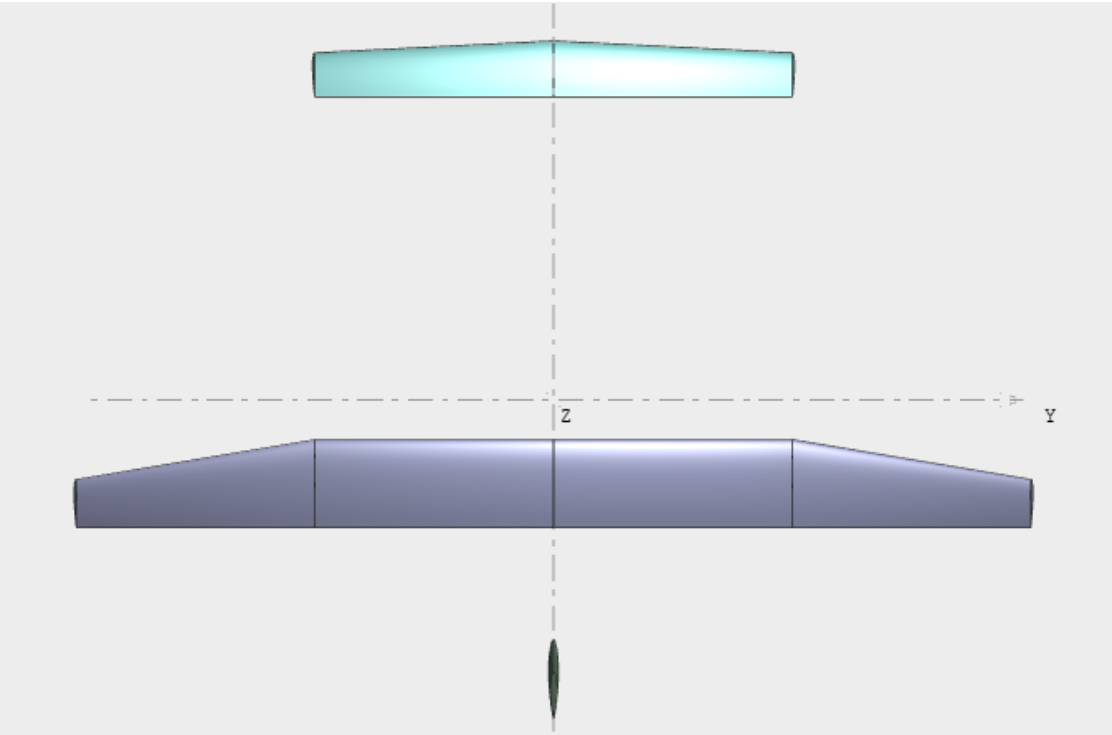

Figure 12: Upper view of the final configuration

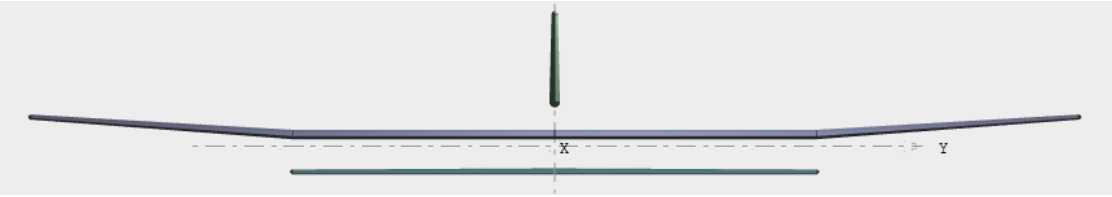

Figure 13: Front view of the final configuration

5 Numerical Aerodynamic Methods

5.1 Flow5 and VLM Methodology

The aerodynamic analysis and design optimization of the UAV were conducted using Flow5, a computational fluid dynamics (CFD) solver rooted in potential flow theory. This software was selected for its capability to rapidly evaluate complex 3D geometries, suitable for the iterative conceptual design phase.

5.1.1 Theoretical Framework: 3D Panel Method

The core solver within Flow5 operates on the assumption of inviscid, incompressible, and irrotational flow. Under these conditions, the velocity vector field $\mathbf{V}$ can be expressed as the gradient of a scalar velocity potential Φ ($\mathbf{V} = \nabla\Phi$). The conservation of mass for an incompressible fluid ($\nabla \cdot \mathbf{V} = 0$) reduces the problem to solving Laplace's equation for the velocity potential throughout the domain:

$$\nabla^2\Phi = 0$$

To solve this equation, Flow5 employs a 3D Panel Method. Unlike the classical Vortex Lattice Method (VLM), which models lifting surfaces as infinitely thin plates with a mean camber line, the method employed in this study utilizes a triangulated mesh approach to discretize the actual 3D surface geometry of the aircraft. This allows for the integration of the fuselage and thick airfoils into a single, watertight volume, enabling the capture of body lift and the specific aerodynamic interference effects critical to canard configurations.[6, 8]

5.1.2 Numerical Discretization: The Linear Galerkin Formulation

The surface of the aircraft is discretized using unstructured triangular panels. To maximize the accuracy of the pressure distribution prediction, particularly near the leading edges where gradients are steep, the analysis utilizes a Galerkin formulation with linear doublet densities.

- **Node-Based Singularities:** Unlike uniform methods which assume a constant singularity strength across a panel surface, the Linear method evaluates doublet densities at the mesh nodes (vertices). The strength is assumed to vary linearly across the face of the triangle between these nodes.
- **Gradient Resolution:** This higher-order formulation provides a continuous distribution of vorticity across panel boundaries. It allows for a precise computation of the surface velocity gradients and Pressure Coefficients (C_p) directly at the nodes, resulting in smooth pressure distribution maps essential for analyzing stall progression and lift distribution.
- **Boundary Conditions:** The solver satisfies the Neumann boundary condition ($\mathbf{V} \cdot \mathbf{n} = 0$) at the collocation points, ensuring zero flow flux through the solid surface of the aircraft.[6]

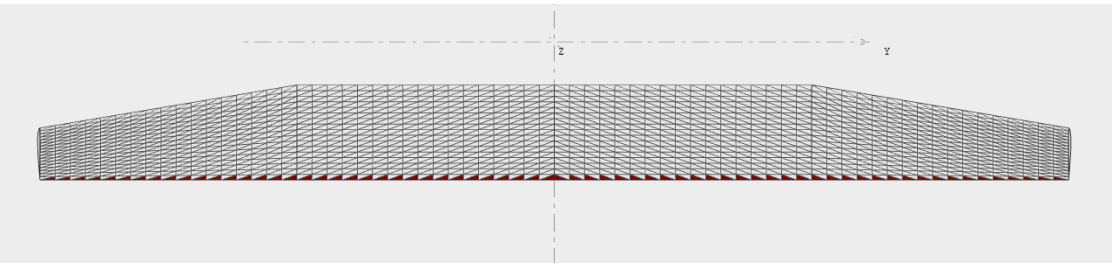

Figure 14: Wing panels

5.1.3 Viscous-Inviscid Interaction

While the potential flow solver is inviscid, viscous effects such as skin friction and form drag are critical for accurate performance prediction at the target Reynolds number range ($Re \approx 10^4 - 10^5$). Flow5 accounts for these effects through a decoupled Viscous-Inviscid Interaction (VII) scheme:

- **2D Polar Generation:** Viscous polars (C_l vs C_d) for the selected airfoils are pre calculated using XFoil, which employs an e^N transition prediction method to model laminar to turbulent transition and laminar separation bubbles.
- **Strip Theory Mapping:** The 3D lifting surfaces are analyzed as a series of streamwise strips. The solver calculates the local effective angle of attack (α_{eff}) and local Reynolds number for each strip using the potential flow solution.
- **Interpolation:** The total viscous drag for the 3D vehicle is derived by interpolating the local drag coefficients from the pre-generated XFoil polar database and integrating them across the span.[6]

5.2 Modeling Assumptions and Limitations

The validity of the numerical results is bounded by specific physical and mathematical assumptions inherent to the potential flow formulation and the specific algorithms used in Flow5.

5.2.1 Assumptions

- **Incompressibility:** The flow is treated as incompressible ($Ma \approx 0$). This is a valid assumption given the vehicle's low-speed mission profile ($V_{cruise} \approx 12 - 15$ m/s).
- **Rigid Wake Model:** For the static stability analysis (Type 7), the wake shed from the trailing edges is modeled as fixed flat panels extending downstream parallel to the

freestream velocity vector. This assumes that wake roll-up does not significantly impact the linear stability derivatives in the cruise condition.

- **Small Perturbations:** The calculation of stability derivatives assumes that the aircraft's response to small disturbances is linear, allowing the flow field to be constructed via linear combinations of elementary unit solutions.[6]

5.2.2 Limitations

- **Finite Difference Derivatives:** Unlike AVL, which calculates stability derivatives analytically, Flow5 evaluates derivatives (e.g., $C_{m\alpha}$) using finite differences. This method perturbs the aircraft's orientation by a small step to compute gradients. While robust for thick surfaces, it requires careful mesh quality control to avoid numerical noise.

- **Post-Stall Behavior:** The potential flow solver does not model flow separation. Consequently, C_L increases linearly with α beyond the physical stall point in the inviscid solution. The analysis is therefore strictly limited to the linear lift regime ($\alpha < 10°$), which covers the intended trim condition ($\alpha_{trim} \approx 2.8°$).

- **Fuselage Interference:** Although the fuselage is modeled geometrically using the linear panel method, the inviscid solver cannot fully capture the separation wake generated by the fuselage body or the complex viscous mixing at the wing-fuselage junction. This may lead to a slight underestimation of the total parasite drag.[6]

5.3 Aerodynamic Coefficients Extraction

Following the convergence of the potential flow solution and the determination of the singularity strengths, the aerodynamic forces and moments acting on the UAV were extracted. Flow5 employs distinct methodologies for calculating lift, induced drag, and viscous drag to maximize numerical accuracy.

5.3.1 Force and Moment Normalization

All aerodynamic coefficients are normalized using the vehicle's reference geometry. The reference parameters defined for the simulation are:

- Reference Area (S_{ref}): 0.117 m^2
- Mean Aerodynamic Chord (MAC): 0.100 m.
- Reference Span (b): 1.20 m.

The longitudinal coefficients are defined as:

$$C_L = \frac{L}{q_\infty S_{ref}}, \quad C_D = \frac{D}{q_\infty S_{ref}}, \quad C_m = \frac{M}{q_\infty S_{ref} MAC}$$

where $q_\infty = \frac{1}{2}\rho V_\infty^2$ is the freestream dynamic pressure.[6]

5.3.2 Lift and Moment Calculation

The lift coefficient (C_L) and pitching moment coefficient (C_m) are derived via near-field surface integration.

- **Pressure Coefficient (C_p):** At each node of the linear triangular mesh, the local velocity magnitude V_{local} is computed from the gradient of the doublet solution. The pressure coefficient is obtained using Bernoulli's equation for incompressible flow:

$$C_p = 1 - \left(\frac{V_{local}}{V_\infty}\right)^2$$

- **Integration:** The total lift and moment are calculated by integrating these pressure forces over the entire wetted surface of the aircraft.

$$\mathbf{F}_{pressure} = \iint_S -C_p q_\infty \mathbf{n}\, dS$$

Unlike standard VLM which often neglects the fuselage's contribution to pitching moment, the 3D Panel Method employed here explicitly integrates pressure forces acting on the fuselage surface. This ensures that the destabilizing fuselage moment ($C_{m_{fus}}$) is accounted for in the trim analysis. [6]

5.3.3 Induced Drag Calculation

For the calculation of induced drag (C_{D_i}), the analysis rejects surface pressure integration in favor of Trefftz Plane integration. Surface integration of drag components is sensitive to mesh discretization errors, which can lead to artificial thrust or inaccurate drag predictions. Instead, Flow5 evaluates the far-field wake. The induced drag is computed by integrating the kinetic energy of the trailing vortices in a transverse plane located infinitely downstream, the Trefftz plane:

$$D_i = \iint_{Trefftz} \frac{1}{2}\rho(v^2 + w^2)\, dA$$

where v and w are the perturbation velocities in the cross-flow plane induced by the wake trace. This method provides a mathematically robust lower bound for the induced drag, essential for optimizing the high-aspect-ratio ($AR \approx 12.3$) planform. [8, 6]

5.3.4 Viscous Drag Formulation

Since the potential flow solver is inviscid, the total drag coefficient (C_D) is constructed by superimposing the viscous drag component ($C_{D,visc}$) derived from the Viscous-Inviscid Interaction (VII) scheme:

$$C_{D,total} = C_{D_i,Trefftz} + C_{D,visc}$$

The viscous component is obtained by interpolating local drag values (C_d) from the Type 1 (fixed speed) XFoil polar database based on the local chord Reynolds number (Re_c) and local lift coefficient (C_l) at each spanwise strip. [6]

5.4 Neutral Point Determination

The determination of the Neutral Point (x_{NP}) was a critical step in ensuring longitudinal stability for the canard configuration. Unlike analytical methods that solve for x_{NP} directly, Flow5 extracts this parameter numerically from the stability derivatives of the full aircraft assembly.[6]

5.4.1 Derivative Calculation

Flow5 calculates longitudinal stability derivatives using a finite difference method, with the necessity of a perturbation approach. To determine the derivatives $C_{m\alpha}$ and $C_{L\alpha}$, the solver performs the following sequence during a Type 7 (Stability) analysis:

1. **Equilibrium Solution:** The solver first converges on the potential flow solution at the trim angle of attack ($\alpha_{trim} \approx 2.8°$).
2. **Perturbation:** The aircraft geometry is virtually pitched by a small increment ($\delta\alpha$) relative to the freestream.
3. **Gradient Calculation:** The derivatives are approximated by the difference quotients.

5.4.2 Mathematical Extraction

The Neutral Point location is extracted from these derivatives using the fundamental stability equation relating the static margin to the slope of the moment curve. The relationship used by the solver is [6]:

$$\frac{dC_m}{dC_L} = \frac{C_{m\alpha}}{C_{L\alpha}} = \frac{x_{NP} - x_{CG}}{MAC}$$

Solving for the Neutral Point position (x_{NP}) using the simulation results for the final configuration, the Neutral Point was computationally identified at $x_{NP} = -0.04$ m.

6 Fuselage and Structural Integration

6.1 Aerodynamic Role of the Fuselage

In the context of a glider, the fuselage is a parasitic aerodynamic component. While it generates negligible useful lift, it contributes significantly to the total parasite drag and actively influences the vehicle's longitudinal and lateral stability. [5] Consequently, the aerodynamic design of the fuselage prioritizes slenderness, minimizing wetted area, and managing flow interference at the wing-body junctions.

6.1.1 Slenderness and Drag Minimization

As illustrated in the preliminary geometric CAD layouts (Figure 15), the fuselage adopts a highly streamlined, slender profile.

By minimizing the maximum frontal cross-sectional area and ensuring gradual curvature changes, the design prevents adverse pressure gradients from triggering premature boundary layer separation, ensuring the flow to remain attached along the length of the fuselage reducing the drag.

Figure 15: Fuselage

6.1.2 The Destabilizing Pitching Moment

Beyond drag generation, the fuselage plays an active role in the aircraft's longitudinal stability. According to slender body theory, a fuselage placed at an angle of attack to the freestream generates an upward force near the nose and a downward force near the tail. [13] While the net lift is near zero, this force couple creates a pure, destabilizing pitching moment ($C_{m,\alpha,fus} > 0$).

Because the fuselage is particularly elongated to provide the necessary moment arms for the canard and the vertical stabilizer, this destabilizing effect is non-negligible. As detailed in Chapter 5, this physical reality justified the use of a 3D Panel Method over a simpler Vortex Lattice Method. The 3D panel analysis accurately captured this destabilizing moment, allowing to reconfigure the aircraft to contrast this new effect generated by the fuselage.

6.1.3 Multi-Surface Integration and Interference

The aerodynamic role of the fuselage also extends to how it manages the integration of the lifting surfaces. The fuselage acts as the central spine establishing the geometric relation between the canard's wake and the main wing.

- **Canard Integration:** The canard is integrated near the nose, where the fuselage boundary layer is thin, ensuring the foreplane to operates in relatively clean, high-energy freestream air.
- **Wing-Body Junction:** The slender profile of the mid-section minimizes the flow acceleration around the fuselage block. This reduces the severity of horseshoe vortices that typically form at the wing-root junction, minimizing interference drag and protecting the lift distribution of the partially tapered main wing. [8]

6.1.4 Quantified Aerodynamic Impact of Fuselage Integration

While the preliminary analysis (Chapter 4) evaluated the isolated lifting surfaces to optimize the clean aerodynamic layout, the physical integration of the fuselage introduces unavoidable aerodynamic penalties. To quantify these effects, the complete fuselage was imported into Flow5 as a 3D STL mesh and connected to the main wing and canard surfaces, allowing the 3D Panel Method to resolve the multi-surface interference and body-lift effects.

The simulation of the complete assembled vehicle revealed significant shifts in both performance and longitudinal trim requirements compared to the idealized model:

1. **Pitching Moment and Canard Re-trimming:** The introduction of the physical fuselage body generated the anticipated destabilizing pitching moment. To counteract this moment and restore a trimmed equilibrium ($C_m = 0$) at the nominal cruise angle of attack ($\alpha \approx 2.9°$), the canard geometric incidence had to be increased from the baseline 1.2° to 1.85°, reaching a new trim angle of ($\alpha \approx 3°$).

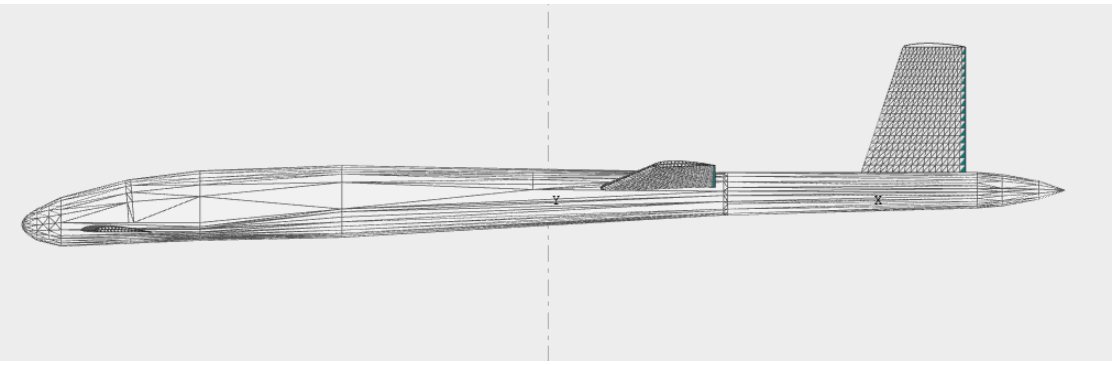

Figure 16: Fuselage mesh

2. **Degradation of Aerodynamic Efficiency:** This required increase in canard incidence carries a direct aerodynamic cost. By forcing the foreplane to operate at a higher local lift coefficient to balance the fuselage, the induced drag of the canard increased. Aggravated by form drag of the fuselage body, and interference drag at the wing-root junctions, the global aerodynamic efficiency experienced a degradation. The new steady-state parameters at trim were extracted as (FIgure 17) :

    - Lift Coefficient (C_L): 0.687
    - Drag Coefficient (C_D): 0.048
    - Aerodynamic Efficiency (L/D): 14.233

3. **Shift in Static Stability:** The 3D volumetric integration of the fuselage also refined the calculation of the vehicle's aerodynamic center. The Flow5 analysis located the final Neutral Point at $x_{NP} = -0.040$ m. Factoring in the finalized mass distribution, this results in an updated Static Margin of 13.86%.

Conclusion on Fuselage Integration:

The numerical data confirms that the fuselage is not aerodynamically neutral. The required adjustment in canard trim ($+0.65°$) and the resulting drop in global efficiency highlight the aerodynamic cost of trim drag in canard configurations. However, the final integrated model achieves a robust static margin (13.86%) and preserves a stable, efficient cruise capability, validating the slender geometric design of the fuselage.

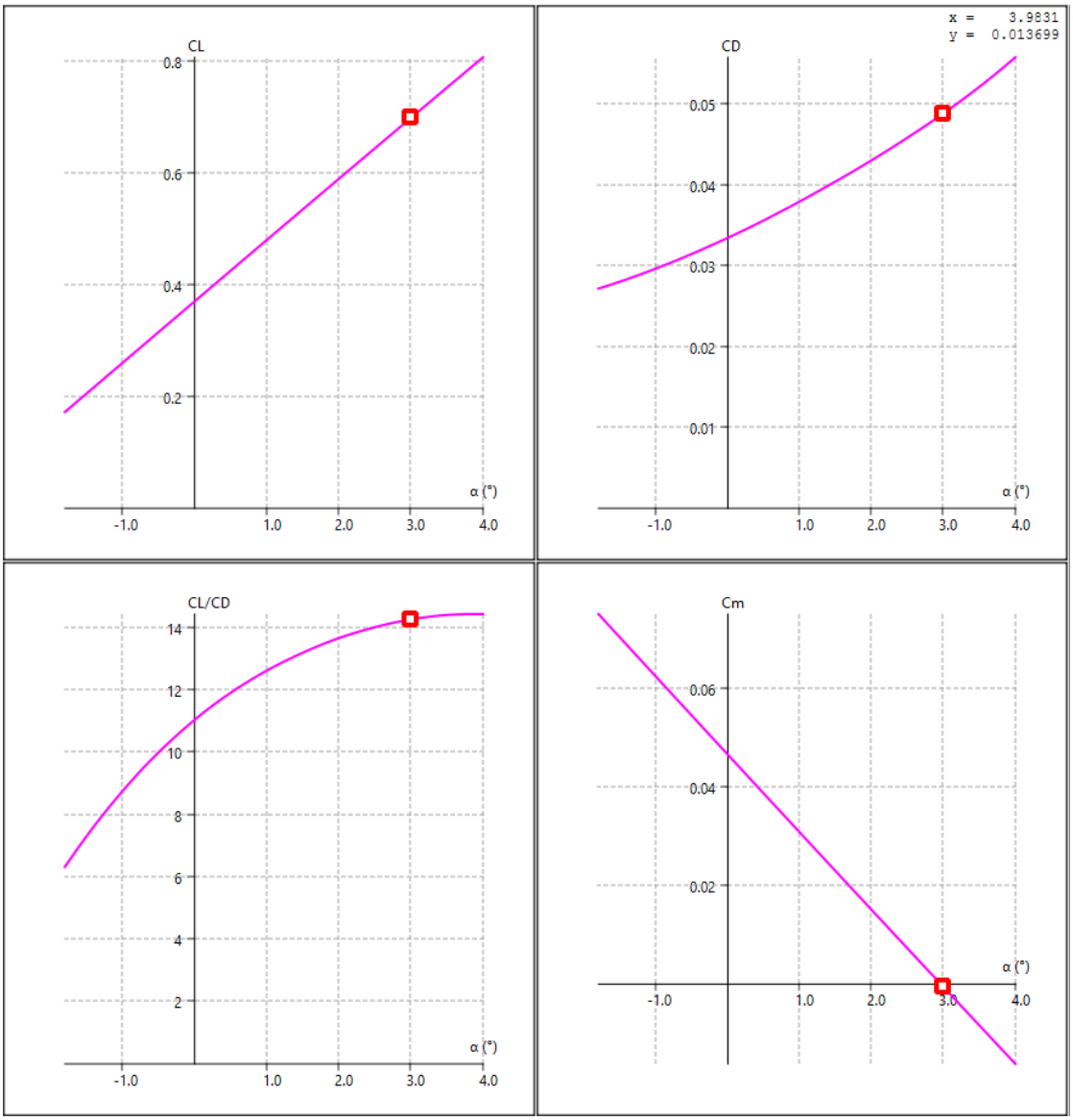

Figure 17: 1. C_L v Alpha 2. C_D v Alpha 3. C_L/C_D v Alpha 4. C_M v Alpha

6.2 Structural Layout and Load Paths

The transition from the external aerodynamic mold line to the internal physical structure requires an analysis of the aerodynamic loads distributed across the airframe. The internal architecture of the UAV, consisting of spars, ribs, and stringers, was designed to absorb and transfer these loads without excessive deformation, ensuring the lifting surfaces to maintain their optimized SD7037 profile under flight stresses.

To determinate the structural sizing, the spanwise aerodynamic loads were extracted from the Flow5 3D panel simulation at the critical cruise trim condition.

6.2.1 Spanwise Lift Distribution and Stall Safety

The structural layout is primarily driven by the spanwise local lift coefficient (C_l), which dictates the vertical shear forces applied to the internal framework. The analysis of the spanwise loading graph (Figure 18) visually confirms the defining safety characteristic of the canard configuration. The foreplane is subjected to a significantly higher aerodynamic loading, peaking at a local lift coefficient of $C_l \approx 0.78$. In contrast, the main wing operates at a more conservative peak of $C_l \approx 0.65$. This load disparity validate the stall safety design of the canard, where it has to work at higher lift coefficients.

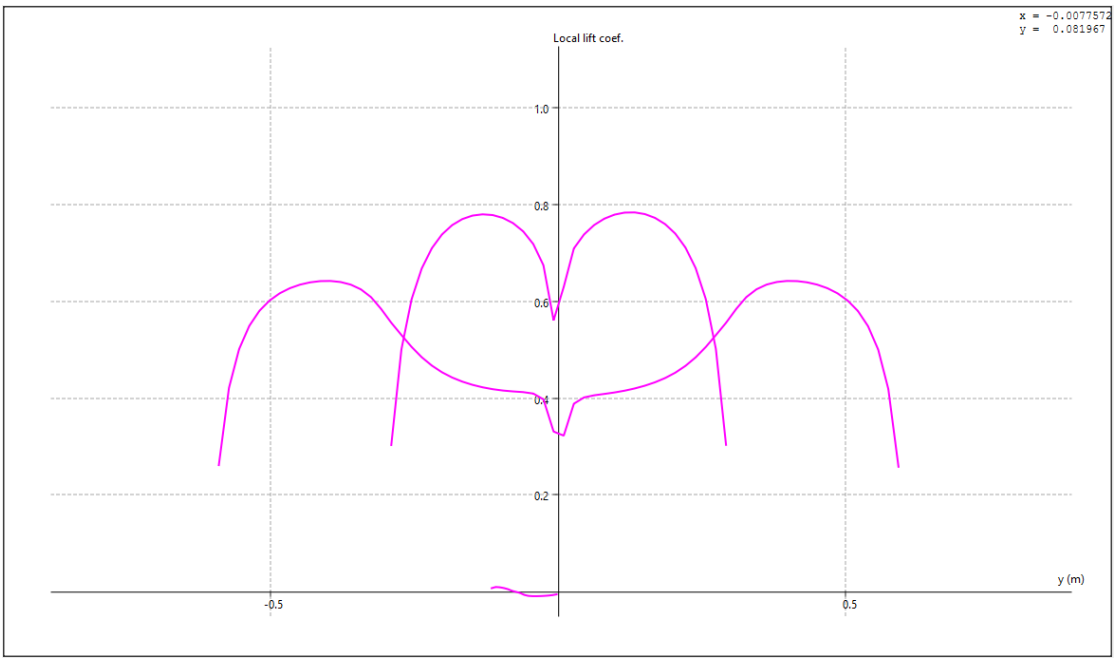

Figure 18: Local lift distribution

Additionally, the lift distribution graph highlights a pronounced dip in lift generation at the

root of the main wing ($y = 0$). This is a direct consequence of the aerodynamic interference from the central fuselage body and the downwash impingement from the highly loaded canard directly upstream. The structural spacing of the root ribs was adapted to account for this turbulent, lower-pressure region.[11]

6.2.2 Bending Moment and Primary Spar Sizing

The most critical structural load acting on an aircraft wing is the bending moment, which attempts to snap the wing at its root.

The Flow5 bending moment graph (Figure 19) for the trim condition indicates a maximum root bending moment of approximately 1.05 N.m for the main wing and 0.2 N.m for the canard. To absorb this load safely, even under dynamic conditions where the load factor increases, the internal layout (Figure21) incorporates a tubular primary spar.

Located near the thickest section of the airfoil (close to the aerodynamic center), this primary spar runs spanwise and anchors into the fuselage stringers. The tubular geometry is efficient at resisting bending stresses while keeping weight to an absolute minimum. Because the bending moment decays almost linearly toward zero at the wingtips ($y = \pm 0.6$ m), the structural mass of the wing can be tapered or lightened outboard without compromising safety, minimizing the roll inertia of the aircraft.[11]

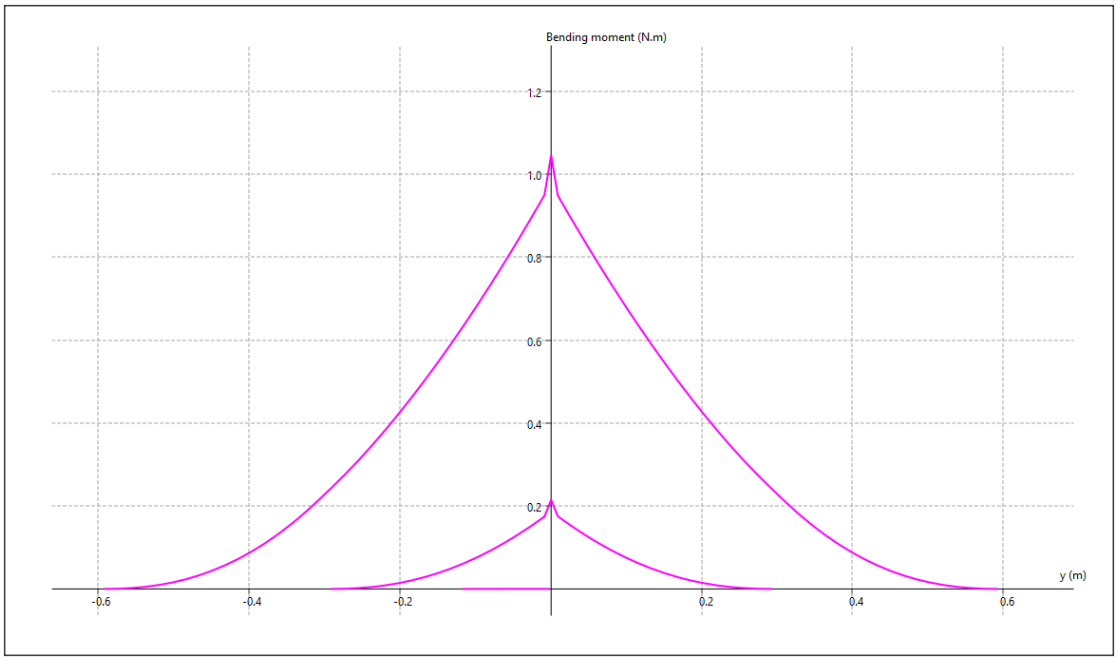

Figure 19: Bending moment

6.2.3 Torsional Loads and Rib Architecture

While the primary spar handles bending, the high-camber SD7037 airfoil introduces a severe secondary challenge: torsion.

As shown in the 1/4 chord pitching moment graph (Figure 20), the inherent camber of the lifting surfaces generates a strong, constant nose-down twisting force along the span, peaking at a coefficient of roughly -0.10. If the wing lacks torsional rigidity, this aerodynamic twisting will physically warp the wing in flight (aeroelastic twist), drastically altering the local angle of attack, increasing drag, and potentially inducing flutter.

To counteract this twisting moment, the CAD structural layout (Figure21) implements a dual-spar architecture. A secondary, lighter spar is positioned aft of the primary tubular spar. Together with the densely spaced aerodynamic ribs, this creates a torsionally rigid box structure. [11]

Furthermore, the rib spacing was optimized to preserve the exact geometric fidelity of the SD7037 profile. Because the upper surface of the airfoil is highly curved and subjected to strong suction peaks, closely spaced ribs prevent the external covering material from sagging inward between the supports in the more loaded areas.

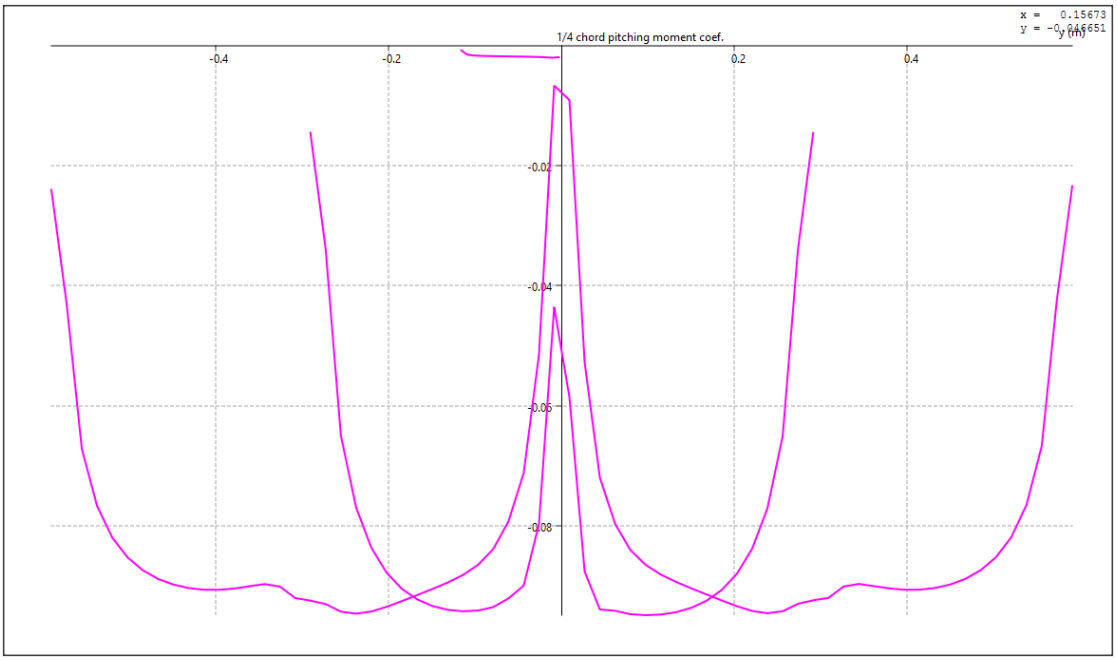

Figure 20: Pitching moment

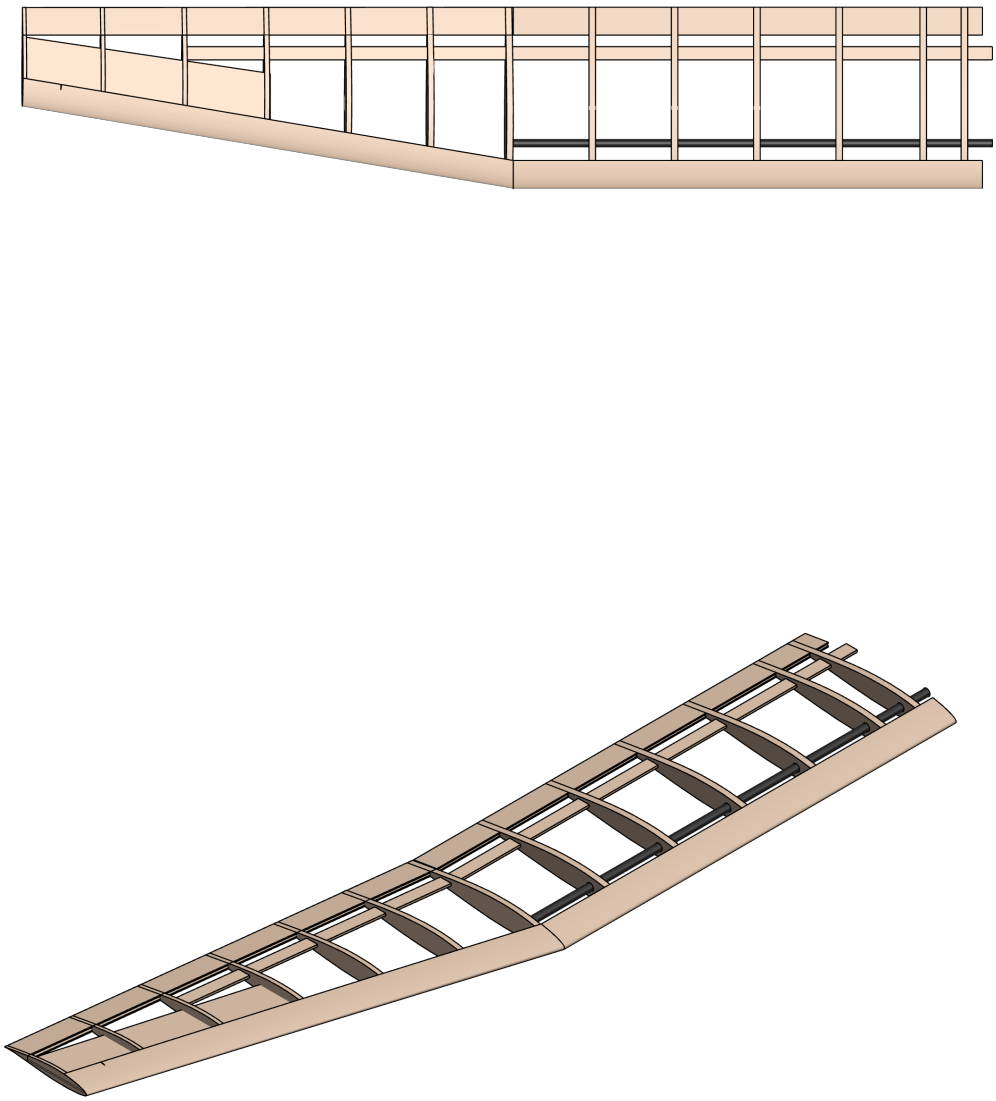

Figure 21: Wing internal structure, upper and diagonal views

6.3 Fuselage Structural Layout and Component Integration

To bridge the gap between the optimized aerodynamic outer mold line and the physical 1.280 kg mass constraint, the fuselage was designed using a lightweight semi-monocoque internal architecture. This structural approach allows the fuselage to house all necessary avionics and propulsion systems while efficiently distributing the flight loads extracted from the Flow5 analysis.

6.3.1 Semi-Monocoque Framework

As illustrated in the internal CAD layout (Figure 23), the fuselage abandons solid-block or thick-walled construction in favor of a stringer-and-former topology.

- **Transverse Formers (Bulkheads):** A series of formers are spaced along the longitudinal axis. These dictate the elliptical aerodynamic shape of the skin and prevent the outer covering from buckling under compressive loads.
- **Longitudinal Stringers:** Connecting the formers are multiple longitudinal stringers spanning from the nose to the tail. These stringers absorb the longitudinal bending moments generated by the fuselage's own destabilizing pitching moment and the aerodynamic loads from the surfaces.

This interlocking skeletal frame provides exceptional torsional rigidity, crucial for maintaining the alignment of the lifting surfaces, while keeping the structural mass fraction strictly within the design limits. [11]

6.3.2 Subsystem Packaging and CG Management

The internal volume of the fuselage is strategically partitioned into dedicated bays. This layout is not merely for organizational convenience; it is the primary mechanism for achieving the precise center of gravity ($x_{CG} = -0.051$ m)

As detailed in the internal structural layout (Figure 23), the components are distributed as follows:

- **Canard Actuation Bay (Purple):** Located at the extreme forward section of the fuselage, this bay houses the control mechanisms and servos required to precisely pitch the all-moving canard foreplane.
- **Forward Battery Compartment (Green):** Positioned in the forward-mid fuselage, ahead of the main wing, this bay is designed to house the primary flight battery pack. Placing this high-density mass well forward is absolutely critical to counteract the heavy moment arm of the rear-mounted propulsion system, ensuring the CG remains safely ahead of the aerodynamic Neutral Point.

- **Roll Control Housing (Dark Red):** Situated centrally at the junction of the main wing roots, these specific structural bays integrate the mounting, routing, and actuation mechanisms for the wing's roll control surfaces.
- **Pusher Propulsion Assembly (Orange):** The electric motor is mounted at the extreme rear of the airframe, driving a pusher propeller through a shaft.

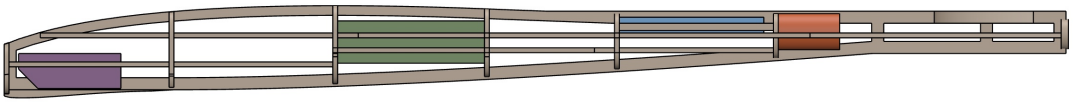

Figure 22: Components layout

6.3.3 Lifting Surface Integration

The structural integrity of the wing-to-fuselage junction is paramount, as it must absorb the peak bending moment of 1.05 N.m.

The CAD design features (Figure 23) a highly robust wing root interface optimized for load distribution. Rather than relying solely on skin adhesion or plugging into a single isolated bulkhead, the primary tubular spars of the main wing are designed to connect directly to a reinforced longitudinal stringer.

This specific structural routing transfers the severe root bending moments and torsional forces from the spars directly into the stringer. The stringer then distributes these stresses longitudinally across multiple transverse formers along the fuselage box. By sharing the load across a larger section of the internal skeleton, the design prevents localized structural failure, minimizes flexing at the wing root, and ensures that the aerodynamic outer skin remains completely unburdened by flight loads. [11]

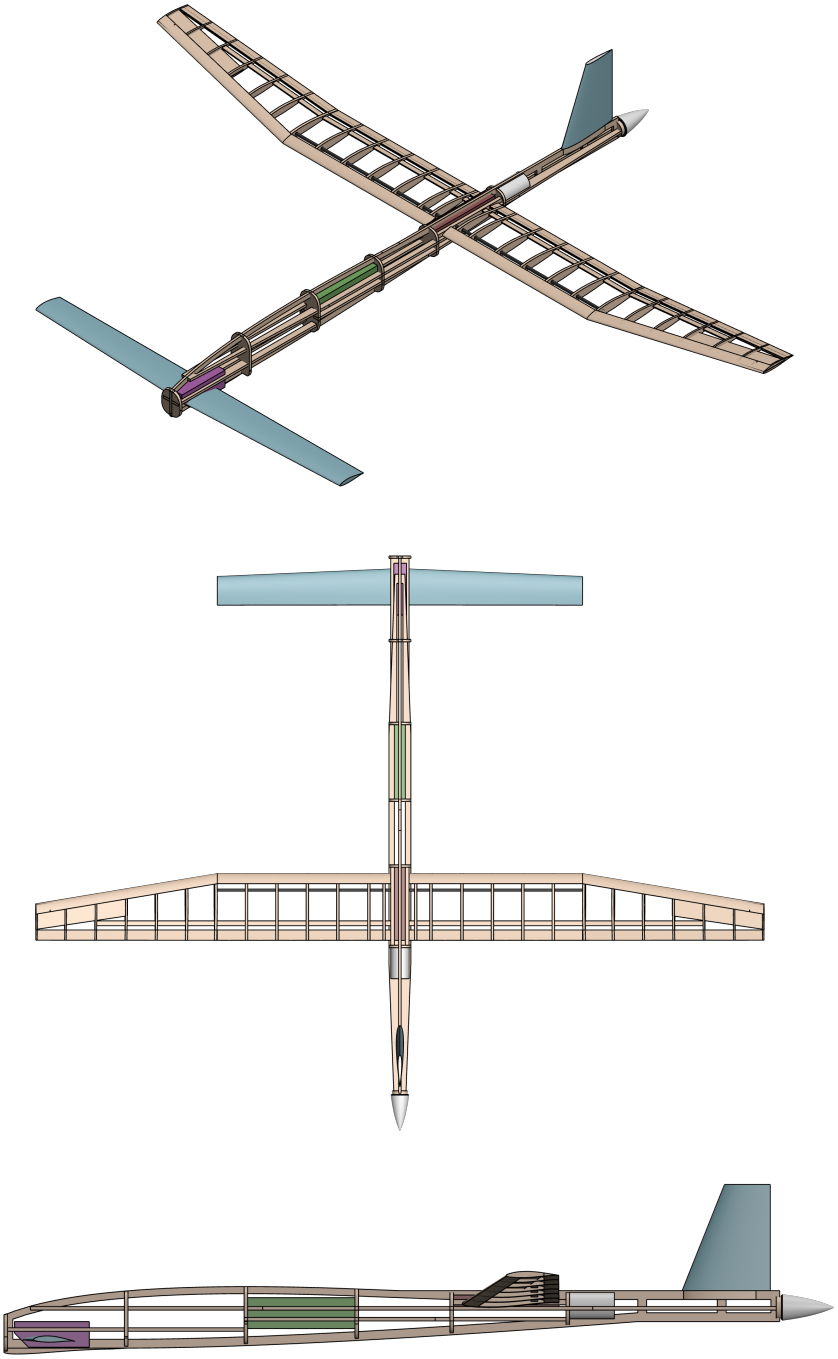

Figure 23: Complete internal structure, diagonal ,upper, and side views

6.4 Materials Selection and Manufacturing Considerations

To realize the semi-monocoque geometry and the optimized aerodynamic profiles while strictly adhering to the 1.280 kg Maximum Take-Off Weight, a hybrid material strategy was adopted. The material selection explicitly assigns specific materials to specific load paths.

6.4.1 Primary Load-Bearing Elements

To counteract the critical bending moments, the primary and secondary wing spars, as well as the canard pivot shaft, are specified as Carbon Fiber Reinforced Polymer (CFRP) tubes.

- **Mechanical Advantage:** Carbon fiber tubes offer exceptional flexural and torsional stiffness at a fraction of the weight of metallic equivalents.
- **Integration:** As detailed in the CAD layout, these carbon tubes act as the central structural arteries, passing continuously through the wooden wing ribs and seamlessly mating with the fuselage stringers to distribute loads globally.

6.4.2 Internal Skeleton

The complex internal skeletal framework, comprising the fuselage formers, longitudinal stringers, and the aerodynamic ribs of the wings and canard, is designed for a mix of balsa wood and aircraft-grade lightweight plywood.

- **Selective Application:** High-density plywood is strategically utilized in high-stress concentration zones.
- **Volume Filling:** For the remainder of the formers and the tightly spaced aerodynamic ribs, low-density balsa wood is utilized. Balsa provides the necessary geometric structure to define the outer mold line without contributing unnecessary parasitic mass.
- **Manufacturing Precision:** To ensure the exact geometric fidelity of the highly sensitive SD7037 airfoil, all wooden components are designed to be manufactured via CNC laser cutting, guaranteeing tight tolerances.

6.4.3 Aerodynamic Skin

Because a fully sheeted wooden or composite skin would violate the mass constraint, the structure framework is designed to be covered with a lightweight heat-shrink polymer film.

- **Aerodynamic Surface:** When activated by heat, this film shrinks tightly across the balsa ribs and stringers, creating a smooth and impermeable surface finish that is ideal for the low-Reynolds-number regime.

- **Torsional Contribution:** While the spars provide the primary torsional rigidity, a properly tensioned shrink film significantly contributes to the overall shear stiffness of the wing box.

6.4.4 Volumetric Analysis and Mass Budgeting

To validate the 1.280 kg Maximum Take-Off Weight (MTOW) established during the conceptual phase, a volumetric analysis was performed on the finalized CAD model. Extracting the volume of the designed components allows for an estimation of the bare airframe mass before to the installation of avionics and propulsion.

The CAD analysis yielded the following exact material volumes:

- **Internal Structure** (Fuselage formers, wing ribs, stringers): $377,942.65$ mm^3 (approx. 377.9 cm^3)
- **External Covering** (Aerodynamic skin): $272,615.28$ mm^3 (approx. 272.6 cm^3)

Mass Implications:
If the internal structure (377.9 cm^3) is manufactured utilizing lightweight aircraft plywood and balsa wood, with an average density ranging from 0.15 to 0.40 g/cm^3, the internal skeleton alone will contribute with 100 to 150 grams to the total weight.

Similarly, the external skin volume (272.6 cm^3) ensures that whether the UAV is covered with a heat-shrink polymer film or a lightweight 3D printed composite shell, the total mass of the aerodynamic envelope remains minimal.

Combining these structural volumes, the airframe is projected to consume less than half of the total mass budget, leaving the vast majority of the 1.280 kg MTOW for the flight battery, the electric motor, and the flight control avionics.

7 Propulsion System Design

7.1 Electric Propulsion for Small UAVs

The propulsion system of the UAV must be carefully matched to the aerodynamic and structural characteristics established in previous chapters. For a glider, the powerplant is technically a secondary system; its primary roles are to launch the vehicle, provide a robust climb rate to reach the designed altitudes, and sustain steady-state cruise only when unpowered flight is not viable. Consequently, the system must deliver high specific power during climbs while imposing an absolute minimum drag and weight penalty during the glide.

The adoption of an electric powertrain provides several engineering advantages over combustion alternatives [4]:

- **Mass and CG Stability:** Unlike combustion systems, which constantly lose mass as fuel is consumed, the mass of an electric battery remains entirely constant throughout the flight. Ensuring that the static margin and the Center of Gravity remain locked in from launch to landing.
- **Structural Safety:** BLDC motors operate with almost zero mechanical vibration, protecting the internal skeleton from high-frequency fatigue.
- **Intermittent Mission Profile Suitability:** The mission profile consists of powered ascents followed by unpowered gliding phases. Electric motors are uniquely suited for this type of operations. They provide instantaneous torque for launch and, can be instantly deactivated or restarted in flight.
- **Propeller Braking:** Modern ESCs (Electronic speed control) feature active electronic braking. When the throttle is cut, the motor is forcefully stopped and held in place. This feature allows a folding propeller to dynamically snap shut against the fuselage, reducing parasite drag during the glide phase.

7.2 Pusher Propeller Configuration Rationale

The physical placement of the propulsion system interfere with the global aerodynamic behavior of the aircraft. For this aircraft, a pusher configuration was selected over a conventional nose-mounted tractor layout. This decision was driven by three primary aerodynamic and operational points:

- **Aerodynamic Cleanliness and Slipstream Management:** The most significant advantage of a pusher configuration is the preservation of undisturbed freestream airflow over the lifting surfaces. A traditional tractor propeller accelerates the air, generating a turbulent, spiraling slipstream that affects directly fuselage and wing roots. This turbulence prematurely changes the boundary layer from laminar to turbulent, increasing the skin friction and interference drag across the airframe. By placing the propeller at the rear, the fuselage, the main wing, and the canard operate in clean air.
- **Optimization of the Unpowered Glide Phase:** Because of the mission requirements, the propulsion system is deactivated for the majority of the flight profile. Therefore, the propeller must generate minimum parasite drag when not in use. When the electronic brake is applied, the aerodynamic drag physically forces the blades to fold backward.

Design Compromises and Mitigation:

The selection of a pusher configuration does introduce two challenges, resolved during the design phase:

- **CG Management:** Placing the mass of the motor at the rear of the aircraft induces a nose-up pitching moment. As detailed in Section 6.3, this was mitigated by subdividing the internal volume and using the flight battery as functional forward ballast to lock in the required CG and static margin.
- **Wake Ingestion:** The propeller operates in the aerodynamic wake of the fuselage and the downwash of the main wing. While this slightly reduces the propulsive efficiency (η_{prop}), the reduction in airframe drag outweighs this propulsive penalty. [13, 4]

7.3 Thrust and Power Requirements

To properly size the electric motor and battery, the minimum propulsive forces required for the different flight phases must be calculated. The analysis is anchored to the designated cruise velocity of 14 m/s. However, because the Flow5 3D panel method predominantly captures induced and form drag while neglecting the viscous skin friction of the fuselage body, this parasitic penalty must first be analytically resolved.

7.3.1 Fuselage Skin Friction Estimation

The boundary layer behavior along the fuselage is dictated by the longitudinal Reynolds number (Re_L). Assuming standard sea-level kinematic viscosity ($\nu \approx 1.5 \times 10^{-5}$ m^2/s), the fuselage length of $L = 0.979$ m, and a cruise velocity of $V = 14$ m/s, the Reynolds number is:

$$Re_L = \frac{V \cdot L}{\nu} = \frac{14 \cdot 0.979}{1.5 \times 10^{-5}} \approx 913{,}733$$

Operating in this regime, and accounting for the wake from the canard, a skin friction coefficient of $C_f \approx 0.004$ is assumed.

To calculate the viscous drag force (D_{visc}), the wetted surface area was extracted from the CAD model ($S_{wet} = 0.1756$ m^2). Using the dynamic pressure ($q = 120.05$ N/m^2) at 14 m/s [2], the physical viscous drag generated by the fuselage isù:

$$D_{visc,fus} = q \cdot S_{wet} \cdot C_f$$

$$D_{visc,fus} = 120.05 \cdot 0.1756 \cdot 0.004 \approx 0.084 \text{ N}$$

7.3.2 Cruise Requirements

In steady, level flight, the thrust (T) must balance the total aerodynamic drag (D_{total}). At the trimmed cruise condition ($\alpha = 3°$), the simulation extracted a baseline drag of 0.684 N (Figure 24). Adding the fuselage skin friction results in a total cruise drag of:

$$D_{cruise} = D_{Flow5} + D_{visc,fus} = 0.684 + 0.084 = 0.768 \text{ N}$$

The mechanical power (P_{mech}) required to maintain this level flight is the product of the required thrust and the freestream velocity [5]:

$$P_{mech,cruise} = T_{cruise} \cdot V = 0.768 \cdot 14 = 10.75 \text{ W}$$

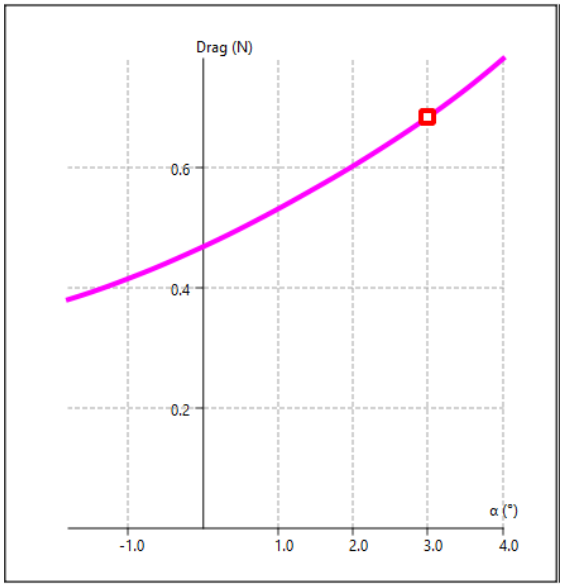

Figure 24: D v Alpha in cruise

7.3.3 Rate of Climb Requirements

For the mission profile, the UAV must be capable of a robust climb rate to gain altitude efficiently. A target vertical climb rate of $V_z = 2.0$ m/s was established.

During a steady climb at flight path angle γ, the thrust must overcome both the total aerodynamic drag and the longitudinal component of the aircraft's weight ($W = m \cdot g = 1.280 \cdot 9.81 = 12.55$ N).

To evaluate the drag during climb (D_{climb}), a dedicated Flow5 simulation (Figure 25) was executed for a trimmed climbing attitude ($C_m = 0$). By deflecting the canard to an incidence of $2°$, the aircraft achieved equilibrium at an angle of attack of $\alpha = 4.1°$, resulting in a higher lift coefficient ($C_L = 0.879$) and an aerodynamic efficiency of $L/D = 14.846$.

The drag extracted from the simulation was 0.837 N. Augmenting this with the fuselage friction penalty (0.084 N) yields a total climb drag of 0.921 N. The required climbing thrust is [5]:

$$T_{climb} = D_{climb} + W \sin(\gamma) = 0.921 + 12.55 \cdot \left(\frac{2.0}{14}\right) = 0.921 + 1.793 = 2.714 \text{ N}$$

The corresponding mechanical power required to sustain this 2.0 m/s climb is:

$$P_{mech,climb} = T_{climb} \cdot V = 2.714 \cdot 14 = 38.0 \text{ W}$$

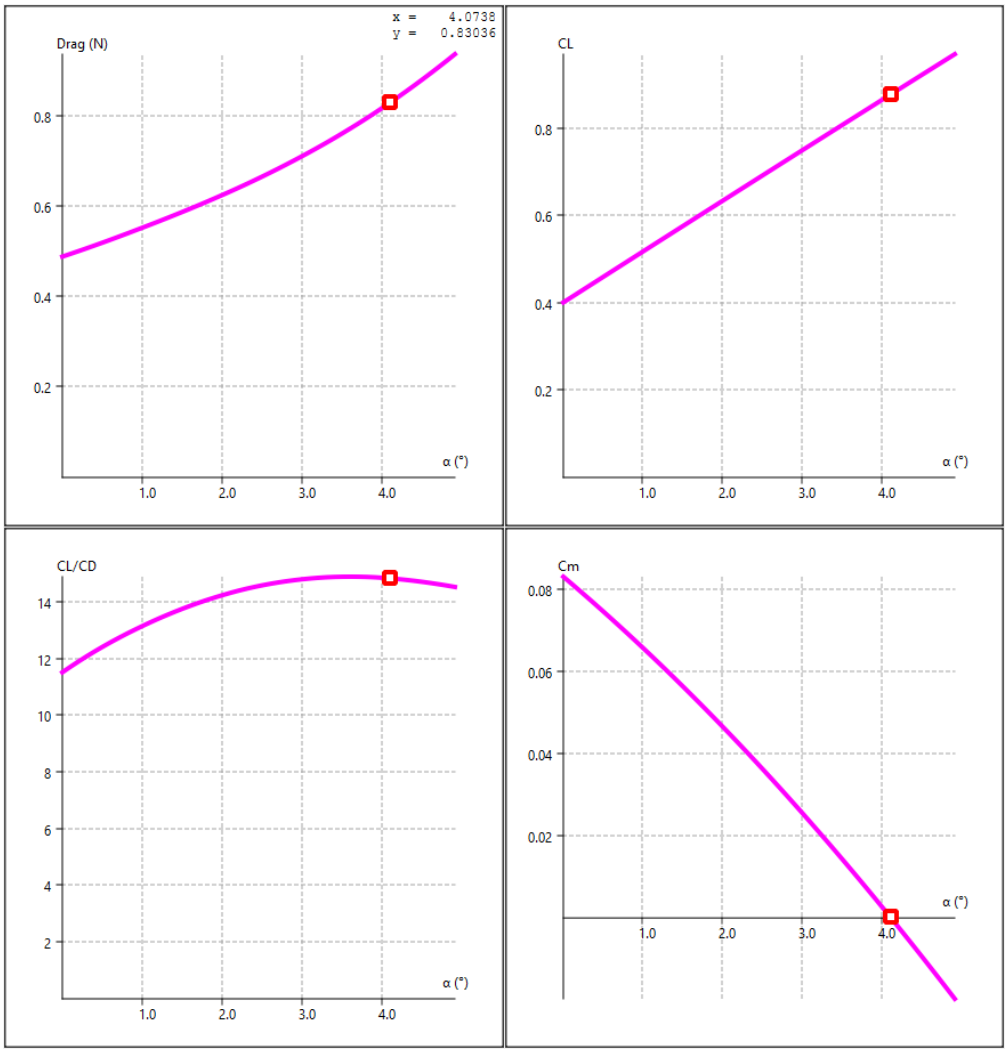

Figure 25: 1. D v Alpha 2. C_L v Alpha 3. C_L/C_D v Alpha 4. C_m v Alpha

7.3.4 Electrical Power Sizing and Efficiency

To determine the actual electrical power (P_{elec}) drawn from the flight battery, the compounding inefficiencies of the propulsion system must be accounted for.

Assuming a conservative combined electromechanical and propeller efficiency of 50% ($\eta_{sys} =$

0.50), the required electrical power is:

$$P_{elec} = \frac{P_{mech,climb}}{\eta_{sys}} = \frac{38.0}{0.50} = 76.0 \text{ W}$$

Conclusion on Power Requirements: Applying a 25% safety margin to account for non-ideal atmospheric conditions and battery voltage sag, the propulsion system must be capable of delivering 100 W of electrical peak power.

7.4 Motor and Propeller Matching

The efficiency of a propulsion system dependents on the matching of the motor's rotational speed to the aerodynamic pitch of the propeller, ensuring the system operates optimally at the target 14 m/s flight velocity.

7.4.1 Propeller Selection and Pitch Speed

The aerodynamic selection of the propeller blades is driven by the necessary pitch speed (V_{pitch}), the theoretical speed at which the propeller would move forward through a solid medium in one revolution.

To generate thrust without stalling the blades, the pitch speed must exceed the 14 m/s cruise velocity. An 8x6 folding propeller (8-inch diameter, 6-inch pitch) is the optimal aerodynamic match for this envelope.

Assuming the motor drives the propeller at a nominal 10,000 RPM under load, the pitch speed can be calculated by converting the 6-inch pitch (0.1524 m) into meters per second:

$$V_{pitch} = \frac{\text{RPM} \cdot \text{Pitch}}{60} = \frac{10000 \cdot 0.1524}{60} = 25.4 \text{ m/s}$$

This pitch speed provides an advance ratio relative to the 14 m/s freestream velocity, allowing the propeller to generate the required 2.71 N of thrust without encountering a "windmilling" condition.[5]

7.4.2 Brushless Motor Sizing (K_v Rating)

To drive the 8x6 propeller at the target RPM, the motor must be matched to a Lithium battery (11.1 V) architecture . Brushless motors are categorized by their K_v rating (RPM per Volt).

To achieve an operational speed of approximately 10,000 RPM under aerodynamic load on an 11.1 V supply, a motor with a specific speed of 1000 to 1200 K_v is required:

$$\text{Theoretical RPM} = K_v \cdot V_{nom} = 1000 \cdot 11.1 = 11{,}100 \text{ RPM}$$

Because the pusher configuration is sensitive to tail weight, the mass of the motor must be minimized to avoid a rearward CG shift. A small stator size in the 2212 or 2306 class, weighing between 35 and 55 grams, represents a balanced compromise.

Motors in this class are rated for 150 W to 200 W of continuous power. By operating a 150 W motor at our calculated 100 W maximum climb requirement, the system will run at peak electromechanical efficiency ($\eta_{motor} > 80\%$) and remain thermally stable, eliminating the risk of overheating during extended altitude-gaining maneuvers.

7.5 Battery Sizing and Flight Endurance

With the mechanical and electrical power requirements established, the energy storage system can be mathematically sized. A 3-cell (3S) Lithium Polymer (LiPo) battery with a nominal voltage of 11.1 V and a capacity of 1500 mAh (1.5 Ah) was selected.

To prove the viability of this selection, the theoretical flight endurance must be calculated for both continuous cruise and a "climb and glide" mission profile.

7.5.1 Total Energy Capacity

The total nominal energy (E_{bat}) stored within the selected LiPo battery is the product of its nominal voltage (V_{nom}) and its charge capacity (C):

$$E_{bat} = V_{nom} \cdot C = 11.1 \cdot 1.5 = 16.65 \text{ Wh}$$

To preserve battery health and prevent chemical degradation, a maximum Depth of Discharge of 80% is assumed. [9] Therefore, the total usable energy (E_{usable}) for the flight is:

$$E_{usable} = E_{bat} \cdot 0.80 = 16.65 \cdot 0.80 = 13.32 \text{ Wh}$$

7.5.2 Continuous Powered Cruise Endurance

While the UAV is designed as a glider, evaluating the maximum continuous powered flight time provides a baseline for its operational range. Using the cruise mechanical power requirement of 10.75 W and an overall system efficiency of $\eta_{sys} = 0.50$, the electrical power drawn during level flight ($P_{elec,cruise}$) is:

$$P_{elec,cruise} = \frac{P_{mech,cruise}}{\eta_{sys}} = \frac{10.75}{0.50} = 21.5 \text{ W}$$

The theoretical endurance in cruise (t_{cruise}) is calculated by dividing the usable energy by the electrical power draw:

$$t_{cruise} = \frac{E_{usable}}{P_{elec,cruise}} = \frac{13.32}{21.5} \approx 0.62 \text{ hours} \approx 37 \text{ minutes}$$

At the nominal cruise speed of 14 m/s, this 37-minute endurance translates to a theoretical powered range of approximately 31 km in calm atmospheric conditions.

7.5.3 Climb and Glide Mission Profile

For this section we considering a mission profile that consist in running the motor at high power to quickly climb to a target altitude, then shutting the motor off to glide.

Assuming a target altitude gain of $\Delta h = 100$ m per climb, at the established vertical climb rate of $V_z = 2.0$ m/s, the time required for one full climb (t_{climb}) is:

$$t_{climb} = \frac{\Delta h}{V_z} = \frac{100}{2.0} = 50 \text{ s}$$

Using the electrical climb power requirement of 76.0 W calculated in Section 7.3, the energy consumed during a single 100-meter climb (E_{climb}) is:

$$E_{climb} = P_{elec,climb} \cdot \left(\frac{t_{climb}}{3600}\right) = 76.0 \cdot \left(\frac{50}{3600}\right) \approx 1.05 \text{ Wh}$$

By dividing the total usable battery energy by the energy required for a single climb, the maximum number of altitude-gaining cycles (N_{climbs}) can be determined [9] :

$$N_{climbs} = \frac{E_{usable}}{E_{climb}} = \frac{13.32}{1.05} \approx 12.6 \text{ climbs}$$

8 Conclusions and System-Level Synthesis

8.1 Architecture Trade-Offs and Synthesis

The development of this UAV required a continuous balancing of aerodynamic performance, longitudinal stability and structural complexity. Aircraft design is fundamentally an exercise in compromise, and the final configuration presented in this thesis is the direct synthesis of several system-level trade-offs made throughout the design phases:

- **Global Configuration and Canard Interference:** The canard configuration was selected because it allows both lifting surfaces to contribute positively to lift generation, sharing the vehicle's weight and reducing the total lift required from the main wing. Additionally, it guarantees passive stall safety, as the canard is designed to stall before the main wing, naturally dropping the nose and preventing stall. However, this architecture required accepting two major aerodynamic compromises: the canard's trailing vortex and downwash impinge upon the main wing, degrading its effective angle of attack and increasing induced drag. Furthermore, to ensure that the canard will stalls first, the main wing can never be utilized at its absolute maximum lift coefficient ($C_{L_{max}}$), which limits the aircraft's minimum speeds.

- **Canard Sizing and Mass Distribution:** Sizing the canard presented a conflict between induced drag and static stability. While increasing the canard's span improves aerodynamic

efficiency and reduces tip vortices, it simultaneously shifts the vehicle's global aerodynamic center forward. This shift reduces the static margin and necessitates additional nose ballast to correct the center of gravity. Consequently, a moderate area ratio with a 0.60 m span was selected to provide sufficient pitch authority without incurring in an excessive structural weight penalty.

- **Main Wing Geometry vs. Manufacturing Complexity:** To minimize induced drag, a fully tapered wing generates an elliptical lift distribution, which is theoretically ideal. However, at a small scale, this planform presents different manufacturing complexities and structural fragility at the narrow wingtips. A fully rectangular wing offers manufacturing simplicity but suffers from poor aerodynamic efficiency due to the tip vortices. The resolved trade-off is a partially tapered planform.

- **Canard Airfoil Selection and Trim Drag:** Control surfaces typically utilize symmetric airfoils, but simulations revealed that a symmetric NACA profile required an inefficient 4.7° geometric incidence to trim the aircraft. Forcing a symmetric profile to such high local angles induces premature boundary layer separation and non-linear aerodynamic behavior. The trade-off was to utilize a cambered SD-series airfoil for the canard, which allows to trim at just 1.2°. The reduced trim drag, prevented flow separation, and improved the whole-aircraft lift-to-drag ratio. Additionally, the nominal cruise trim was deliberately restricted to 2.85° rather than higher angles to preserve the canard's stall safety margin and prevent its deflected wake from impinging directly onto the main wing.

- **Lateral-Directional Stability Devices:** While winglets can reduce induced drag and provide directional stability, they also add structural mass to the wing extremities, increasing roll inertia. Moreover, at low Reynolds numbers, the sharp junctions of winglets can trigger localized flow separation. Consequently, winglets were discarded. To provide passive roll stability, a 4° dihedral was integrated into the main wing, which actively resists spiral divergence. The penalty for this dihedral is a strong roll-yaw coupling that induces a lightly damped Dutch roll oscillation. To suppress this without excessive complexity, a single central vertical stabilizer was sized and positioned at the aft, accepting a slightly reduced Dutch roll damping to secure the aggressive roll stability necessary for an autonomous UAV.

- **Pusher Propulsion and CG Management:** The selection of a pusher propulsion system was driven by the need to preserve undisturbed freestream airflow over the canard and main wing, eliminating turbulent propwash from tripping the boundary layer. The aerodynamic trade-off is wake ingestion: the propeller must operate in the turbulent wake of the fuselage and main wing downwash, which reduces propulsive efficiency. Furthermore, mounting the motor mass at the rear induced a nose-up pitching moment. To counteract this and lock in

the static margin, mass centralization was sacrificed. The internal volume was partitioned to utilize the flight battery as functional ballast in the forward bay, balancing the CG without the need for dead weights.

8.2 Summary of Achievements

The primary objective of this thesis, to conceptualize, design, and numerically validate an UAV has been successfully met. The analytical methods and simulations confirm that the final architecture satisfies all initial design constraints. The key achievements of this study are summarized as follows:

- **Aerodynamic Performance and Sink Rate:** Through iterative geometric refinement and the selection of the SD7037 airfoil, the aircraft demonstrates strong gliding capabilities. Operating at 2.85° in trim condition, the fully assembled vehicle generates a lift coefficient (C_L) of 0.687 and a drag coefficient (C_D) of 0.048. This results in an aerodynamic efficiency of $L/D \approx 14.2$. Furthermore, the configuration achieves a predicted minimum sink rate of 1.12 m/s.

- **Passive Longitudinal and Lateral-Directional Stability:** The instability risks of the canard configuration were resolved across all axes. Longitudinally, the final mass distribution places the center of gravity at $x_{CG} = -0.051$ m, ahead of the neutral point at $x_{NP} = -0.040$ m. This provides a static margin of 13.86% for the fully assembled geometry. The spanwise lift distribution verified that the foreplane ($C_l \approx 0.78$) will stall before the main wing ($C_l \approx 0.65$), guaranteeing a passive pitch response. Laterally, the integration of a 4° main wing dihedral ensures rapid roll subsidence ($C_{l\beta} < 0$) to resist spiral divergence. The resulting yaw-roll coupling is managed by a centrally mounted vertical stabilizer, which provides the necessary static directional stability ($C_{n\beta} > 0$) to passively damp Dutch roll oscillations.

- **Structural Integration and Load Management:** The internal architecture was designed to manage the severe aerodynamic loads extracted from the simulations.

  - **Bending Loads:** At trim condition, the main wing experiences a peak root bending moment of 1.05 N.m, while the canard root experiences 0.2 N.m. To absorb this, the design utilizes a primary Carbon Fiber Reinforced tubular spar. At the wing-root interface, this spar connects directly to a reinforced longitudinal stringer, distributing the severe bending moments across multiple transverse formers within the fuselage.

  - **Torsional Loads:** The airfoil generates a constant nose-down twisting force along the span, peaking at a 1/4 chord pitching moment coefficient of roughly -0.10. To prevent aeroelastic twist, a dual-spar architecture was implemented. By pairing the

primary spar with a secondary aft spar and densely spacing the balsa wood ribs, the structure forms a torsionally rigid box.

  - **Mass constrains:** Volumetric CAD analysis confirms that this highly robust bare airframe consumes less than half of the total mass budget, ensuring the 1.280 kg MTOW limit is respected.

- **Propulsion Sizing and Mission Endurance:** The aerodynamic cleanliness of the platform reduces the mechanical power required for cruise to 10.75 W. To sustain a 2.0 m/s climb, the electrical power draw is limited to 76.0 W, allowing the integration of a lightweight (35–55 g) brushless motor. Powered by a 1500 mAh (11.1 V) flight battery, the UAV is capable of performing over 12 full 100-meter "climb and glide" cycles, and a range of $31km$ of powered cruise.

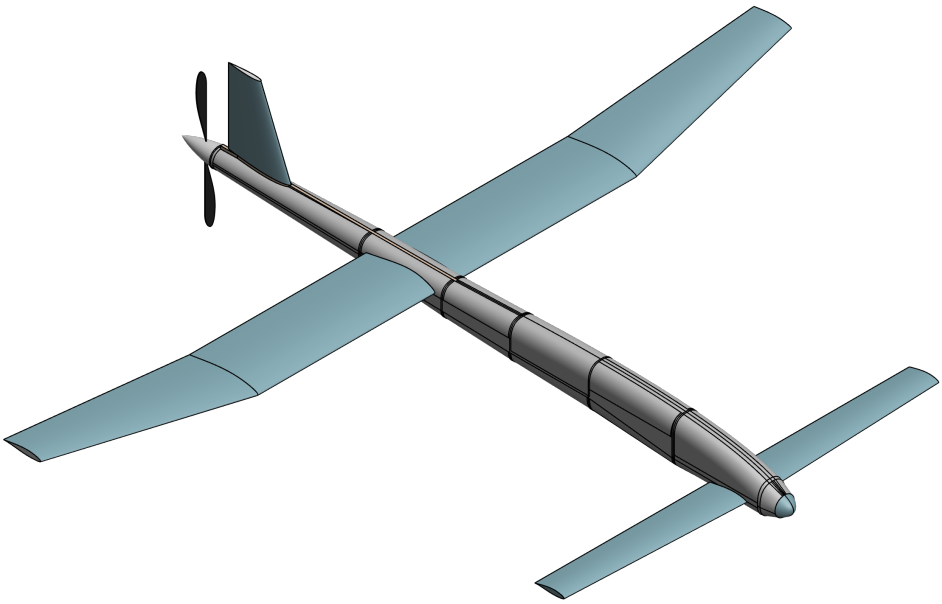

Figure 26: Complete UAV diagonal view

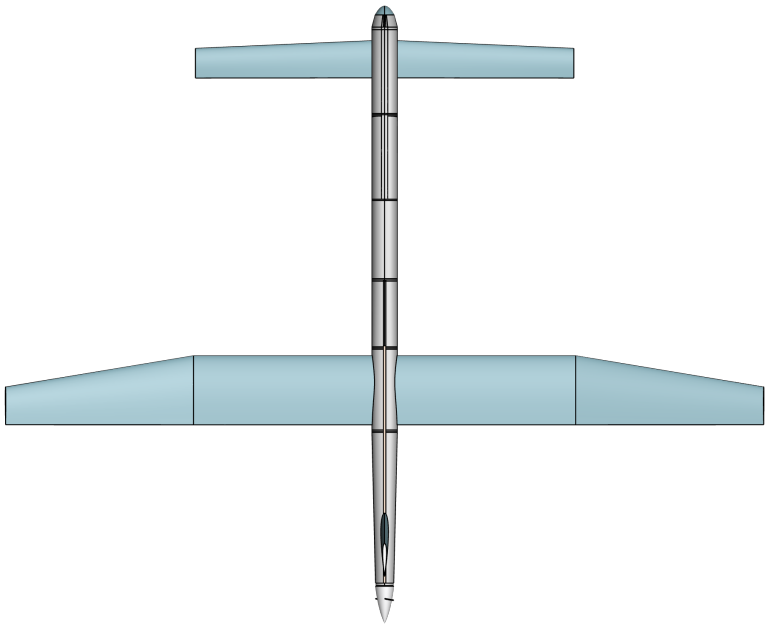

Figure 27: Complete UAV upper view

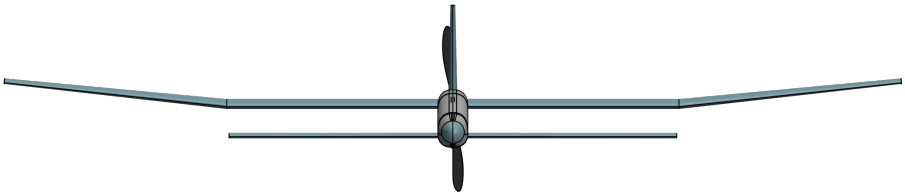

Figure 28: Complete UAV front view

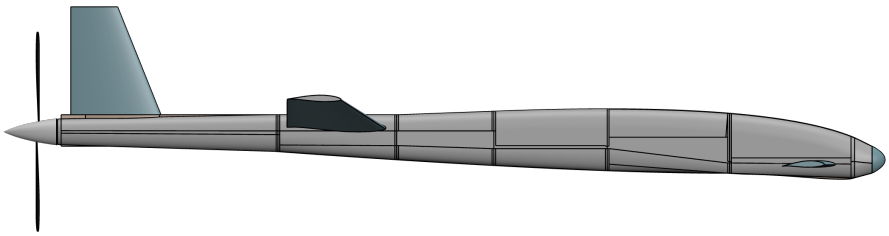

Figure 29: Complete UAV lateral view

Figure 30: Rendering

Category	Parameter	Final Value
Global Specifications	Global Architecture	Canard Monoplane
	Maximum Take-Off Weight	1.280 kg
Main Wing Geometry	Selected Airfoil	SD7037
	Planform Shape	Partially Tapered
	Maximum Wingspan	1.20 m
	Reference Area (S)	0.117 m^2
	Mean Aerodynamic Chord	0.100 m
	Root / Tip Chord	0.11 m/0.06 m
	Aspect Ratio (AR)	≈ 12.3
	Dihedral Angle	4°
Canard Geometry	Selected Airfoil	SD7037
	Planform Shape	Slightly Tapered
	Span	0.60 m
	Root / Tip Chord	0.070 m/0.055 m
	Vertical Offset	-0.04 m
Fuselage & Empennage	Fuselage Length	0.979 m
	Fuselage Wetted Area	0.1756 m^2
	Structural Architecture	Semi-Monocoque
	V-Stab Airfoil	NACA 0012-34
	V-Stab Root / Tip Chord	0.10 m/0.06 m
	V-Stab Span	0.12 m
Propulsion System	Motor Class	35–55g (1000-1200 K_v)
	Propeller	8x6 Folding Pusher
	Flight Battery	3S LiPo (11.1 V, 1500 mAh)
	Target Climb Rate	2.0 m/s
	Cruise Mechanical Power	10.75 W

Table 1: Summary of final geometric and structural parameters for the UAV.

Category	Parameter	Final Value
Flight Envelope	Target Cruise Velocity	14 m/s
	Operating Reynolds Number	$Re \approx 10^4 - 10^5$
Stability Margins	Center of Gravity (x_{CG})	-0.051 m
	Aerodynamic Neutral Point (x_{NP})	-0.040 m
	Static Margin (SM)	13.86%
Integrated Aerodynamics	Nominal Trim Angle of Attack (α)	$\approx 2.9^\circ$
	Canard Geometric Incidence Trim	1.85°
	Lift Coefficient at Trim (C_L)	0.687
	Total Drag Coefficient at Trim (C_D)	0.048
	Final Aerodynamic Efficiency (L/D)	14.23
	Minimum Sink Rate (V_z)	1.12 m/s
Endurance & Autonomy	Continuous Powered Cruise Time	≈ 37 minutes
	Continuous Powered Cruise Range	31 km
	Available 100 m Climb Cycles	12.6 climbs

Table 2: Summary of final aerodynamic and performance characteristics

8.3 Limitations of the Current Study

While the computational models and structural calculations provide a robust baseline for the UAV's conceptual and preliminary design, a mature engineering assessment requires acknowledging the limitations of the employed methodologies. The validity of the numerical results is bounded by the specific physical and mathematical assumptions inherent to the selected tools:

- **Inviscid Flow and Post-Stall Limitations:** The aerodynamic analysis relies primarily on the potential flow solvers (3D Panel Method and VLM) within Flow5. Because the core solver is inviscid, it cannot model flow separation. Consequently, the calculated lift coefficient (C_L) continues to increase linearly beyond the physical stall point, limiting the validity of the aerodynamic data to the linear lift regime (angles of attack below 10°). While sufficient for the nominal 2.85° cruise trim, stall behavior and ultimate maximum lift capabilities cannot be accurately captured using this method.
- **Fuselage Interference Drag Underestimation:** Although the fuselage is geometrically modeled using the linear 3D panel method, the inviscid nature of the solver cannot fully capture the viscous mixing and separation wakes that occur at the wing-fuselage and canard-fuselage junctions. While the Viscous-Inviscid Interaction (VII) scheme interpolates 2D airfoil drag, the unmodeled 3D boundary layer interference may lead to a slight underestimation of the vehicle's total parasite drag in real world conditions.
- **Stability Derivative Extraction Methods:** The calculation of the critical longitudinal stability derivatives (such as $C_{m\alpha}$ and $C_{L\alpha}$), which dictate the neutral point location, relies on a finite difference method. This method perturbs the aircraft's orientation by a small step to compute gradients. While robust, this approach is highly sensitive to mesh discretization errors and can introduce numerical noise if the triangulated surface mesh quality is not strictly controlled.
- **Rigid Wake Assumption:** For the static stability analysis, the solver assumes a rigid wake model where the wake shed from the trailing edges extends downstream purely parallel to the freestream velocity vector. This assumption dictates that dynamic wake roll-up and its shifting influence on the downstream main wing and vertical stabilizer are not fully captured, which could slightly alter the stability derivatives outside of the immediate cruise condition.
- **Rigid Body Dynamics Assumption:** The aerodynamic coefficients and stability margins were extracted assuming a perfectly rigid airframe. Although the structural design utilizes spars and a torsionally rigid box to minimize flexing, a high-aspect-ratio wing ($AR \approx 12.3$) will inevitably experience some degree of aeroelastic deflection under dynamic flight loads. This physical bending and twisting could slightly alter the local angle of attack and the exact trim condition calculated in the rigid numerical model.

8.4 Future Work

This thesis successfully establishes a robust conceptual and preliminary aerodynamic baseline for the high-efficiency canard UAV. However, as certain aspects such as detailed structural finite element analysis, physical flight testing, and advanced active control loops were outside the primary scope of this aerodynamic study, several critical phases of future development are required to transition this design into a fully operational platform:

- **High-Fidelity CFD Validation:** To resolve the uncertainties associated with the inviscid potential flow solver and accurately quantify the viscous interference drag at the wing-fuselage and canard-fuselage junctions, a full Navier-Stokes Computational Fluid Dynamics (CFD) analysis should be conducted. Utilizing high-fidelity solvers (such as ANSYS Fluent or OpenFOAM) will allow for the accurate prediction of deep-stall behavior, boundary layer separation, and the exact trajectory of the canard's turbulent wake at high angles of attack.

- **Flight Control System Integration (Model-Based Design):** While the passive stability of the platform has been numerically verified, the UAV requires active control. Future work must focus on the physical implementation of the flight control architecture utilizing a Model-Based Design approach. The control logic, specifically tailored to the pitch actuation of the all-moving canard, should be developed, tuned, and simulated within the MATLAB/Simulink environment using the aerodynamic stability derivatives extracted from Flow5. This control architecture can then be compiled and deployed directly onto an Arduino-based microcontroller.

- **Physical Prototyping and Construction:** The immediate next step is the physical realization of the UAV. Utilizing the established CAD geometry and the selected materials (CNC laser-cut balsa, aircraft plywood, CFRP tubes, and heat-shrink polymer film), a subscale flying prototype must be constructed. This phase will definitively validate the volumetric mass budgeting and ensure the physical center of gravity precisely matches the calculated $x_{CG} = -0.051$ m requirement.

- **Flight Testing and System Identification:** The ultimate validation of this design will be empirical flight testing. By instrumenting the Arduino prototype with onboard telemetry, real-world data regarding the actual minimum sink rate, the L/D ratio, and the lightly damped Dutch roll oscillations can be recorded. This flight data will be used to calibrate and correct the initial Flow5 aerodynamic models, closing the iterative design loop and proving the real-world viability of the pusher-canard architecture.

References

[1] Airfoil Tools. Airfoil tools database. `http://airfoiltools.com/`, 2024.

[2] John D. Anderson. *Fundamentals of Aerodynamics*. McGraw-Hill Education, 5th edition, 2010.

[3] Seth B. Anderson. A look at handling qualities of canard configurations. Technical Report NASA TM-88354, National Aeronautics and Space Administration, 1986.

[4] Reg Austin. *Unmanned Aircraft Systems: UAVs Design, Development and Deployment*. John Wiley & Sons, 2010.

[5] Carlo Casarosa. *Meccanica del volo*. Plus-Pisa University Press, 2010.

[6] Flow5 Team. Flow5 technical documentation and validation. `https://flow5.tech/docs/flow5_doc/flow5_doc.html`, 2024.

[7] Blair B. Gloss. Effect of canard location and size on canard-wing interference and aerodynamic-center shift related to maneuvering aircraft at transonic speeds. Technical Report NASA TN D-7505, National Aeronautics and Space Administration, 1974.

[8] Ilan Kroo. *Applied Aerodynamics: a digital textbook*. Desktop Aeronautics, 1996.

[9] David Linden and Thomas B. Reddy. *Handbook of Batteries*. McGraw-Hill, 3rd edition, 2002.

[10] Tad McGeer and Ilan Kroo. A fundamental comparison of canard and conventional configurations. *Journal of Aircraft*, 20(11):983–992, 1983.

[11] Thomas H. G. Megson. *Aircraft Structures for Engineering Students*. Butterworth-Heinemann, 5th edition, 2012.

[12] Thomas J. Mueller and James D. DeLaurier. Aerodynamics of small vehicles. *Annual Review of Fluid Mechanics*, 35(1):89–111, 2003.

[13] Daniel P. Raymer. *Aircraft Design: A Conceptual Approach*. American Institute of Aeronautics and Astronautics, 5th edition, 2012.

[14] Burt Rutan. The solitaire. *Soaring*, 46(12):22–26, 1982.

[15] Fred Thomas. *Fundamentals of Sailplane Design*. College Park Press, 1999.